Supporting Information

A Telescoping View of Solute Architectures in a Complex Fluid System

Ryuhei Motokawa,* Tohru Kobayashi, Hitoshi Endo, Junju Mu, Christopher D. Williams, Andrew J. Masters,* Mark R. Antonio, William T. Heller, and Michihiro Nagao

*To whom correspondence should be addressed.

E-mail: motokawa.ryuhei@jaea.go.jp (R.M.); andrew.masters@manchester.ac.uk (A.M.)

CONTENT

1. Method

Materials. TBP (Tokyo Chemical Industry Co., Ltd., Tokyo, Japan; purity, >99%), *n*-octane (Wako Pure Chemical Industries, Ltd., Osaka, Japan; purity, >98%), and deuterated *n*-octane (*n*-octane-d_{18}; Sigma-Aldrich Japan, Tokyo, Japan; purity, >98%) were dried overnight over 4 Å molecular sieves (Wako) before use. Water was deionized using a Millipore Milli-Q purification system (Merck Millipore, Billerica, MA). Nitric acid and ammonia solution were purchased from Wako and used as received. Zirconium(IV) chloride ($ZrCl_4$) anhydrous powder (purity, >99.9%) was purchased from Kojundo Chemical Laboratory Co., Ltd. (Tokyo, Japan) and used as received.

Sample preparation and chemical composition analysis. Aqueous phases of 10.5 M nitric acid solution containing $Zr(NO_3)_4$ were prepared as follows.[41] $ZrCl_4$ powder (12 g) was dissolved in 25 mL of 0.5 M aqueous nitric acid solution in a 300 mL round bottom flask. To this was added dropwise an aqueous ammonia solution under stirring at 80 °C to pH > 10, resulting in the precipitation of hydrated ZrO_2. The precipitate was collected and washed with the aqueous ammonia solution, and then concentrated HNO_3 aqueous solution was added to dissolve the precipitate thoroughly. After the solution was evaporated to remove excess HNO_3, water was added to prepare a stock solution of $Zr(NO_3)_4$ in aqueous nitric acid. The concentrations of $Zr(NO_3)_4$ and HNO_3 in the stock solution were determined as 1.08 and 6.31 M, respectively, by inductively coupled plasma atomic emission spectroscopy (ICP-AES; SII SPS3500, SII Nano Technology Inc., Japan) and potentiometric titration (see section no. 9 of

this Supporting Information file). Aliquots of $[Zr(NO_3)_4]_{aq,in}$ ranging from 0 to 0.049 M in 10.5 M nitric acid solution were prepared by the addition of an appropriate amount of concentrated HNO_3 aqueous solution and water. Note that when $[HNO_3] > 3$ M, the concentrations of polymerized and hydroxylated zirconium are much less than that of $Zr(NO_3)_4$.[69] In fact, the coordination structure of the zirconium complex species in the aqueous, initial phase was confirmed as $Zr(NO_3)_4(H_2O)_{1.3}$ by using EXAFS measurement and its data analysis (see section no. 10 of this Supporting Information file). Additionally, hydroxylated zirconium is not extracted by TBP under any conditions[41] and, if present, remains in the aqueous phase. On the other hand, 0.5 M TBP in *n*-octane-d_{18} is typically used for initial organic phases in the solvent extraction process. All samples containing the $Zr(NO_3)_4(TBP)_2$ complex[70] were then prepared by conducting the biphasic solvent extraction as described in the results section. Note that the primary purpose for using *n*-octane-d_{18} as a diluent in the solvent extraction step is to ensure sufficient neutron scattering contrast between the solutes and the diluent and to minimize the incoherent scattering background due to hydrogen. However, *n*-octane-d_{18} was used for consistency in the EXAFS experiments conducted in this study.

Following solvent extraction, $[Zr(NO_3)_4]_{aq,eq}$ was measured by ICP-AES to confirm $[Zr(NO_3)_4(TBP)_2]_{org,eq}$. In addition, $[Zr(NO_3)_4(TBP)_2]_{org,eq}$ was evaluated by conducting ICP-AES measurements of a back-extracted aqueous solution containing 0.2 M ammonium oxalate, and $[Zr(NO_3)_4(TBP)_2]_{org,eq}$ was consistent with the estimation described above. $[HNO_3]_{org,eq}$ was estimated by measuring the residual HNO_3 in the aqueous phase using the procedure described above (see section no. 9 of this Supporting Information file). $[H_2O]_{org,eq}$ was directly

measured using a Karl Fischer titration apparatus (AQV-2200A, Hiranuma Sangyo Co., Ltd., Japan). $[TBP]_{org,eq}$ was calculated from $[Zr(NO_3)_4(TBP)_2]_{org,eq}$, since $[TBP]_{org,eq} = [TBP]_{in} - 2\cdot[Zr(NO_3)_4(TBP)_2]_{org,eq}$, where $[TBP]_{org,in} = 0.5$ M.

The value of $d_{Zr(NO3)4(TBP)2} = 1.116$ g/mL, which is used for calculating $\phi_{Zr(NO3)4(TBP)2}$ in the organic phase, was directly measured using a density meter (DMA-4500M, Anton Paar Co., Ltd., Graz, Austria), where $\phi_{Zr(NO3)4(TBP)2} = C_{Zr(NO3)4(TBP)2}/d_{Zr(NO3)4(TBP)2}$. $C_{Zr(NO3)4(TBP)2}$ is the concentration of $Zr(NO_3)_4(TBP)_2$ in the organic phase.

EXAFS measurements. EXAFS measurements using quick-scan mode (QXAFS) were performed at the BL11XU beamline of SPring-8, Japan.[71] The incident X-ray beam was monochromatized with a double-crystal Si(111) monochromator using a liquid nitrogen cooling system, and the monochromator was continually moved during the measurements, in contrast to the conventional step-scan method. Data collections were performed in transmission mode. In QXAFS, a measurement time as long as 5 min is typically required for one scan with an X-ray energetic range from 17.59 keV to 19.49 keV (Zr K-edge; $E_0 = 18.00$ keV) when the measurement is repeated 10 times for each sample to accumulate statistically sufficient EXAFS data. All extracted organic solutions from samples no. 1 to 5 and an aliquot of the aqueous phase prior to extraction were loaded into plastic cells with 1-mm-thick walls and a 10 mm sample thickness. All EXAFS data were acquired at 20 °C.

EXAFS data were examined by using analysis code Win-XAS ver. 3.2 developed by Ressler[72] and EXAFS simulation code FEFF ver. 8.4[54]. $k^3\chi(k)$ was obtained by pre-edge

background removal using the Victoreen function and extraction of the EXAFS signal using cubic spline. The EXAFS function was Fourier transformed to calculate $|\mathrm{FT}[k^3\chi(k)]|$ and $\mathrm{Im}\{\mathrm{FT}[k^3\chi(k)]\}$. A Bessel function was used to reduce termination error in the Fourier transform. Theoretical phase shifts and back scattering amplitude functions were calculated using FEFF ver. 8.4[54].

SANS measurements. SANS measurements were performed with the time-of-flight extended q-range SANS (EQ-SANS) diffractometer[73] installed at BL-6, Spallation Neutron Source (SNS), at Oak Ridge National Laboratory, USA. EQ-SANS covers a q range of 0.15 $nm^{-1} < q < 10$ nm^{-1} at a sample-to-detector distance of 1.3 m with a single band of λ ranging from 0.10 nm to 0.56 nm. The divergence of the incident beam was defined by using a 25-mm-diameter source aperture and a 10-mm-diameter sample aperture. The scattered neutrons were detected with a two-dimensional position-sensitive ^{3}He detector of 1.0 × 1.0 m^2 composed of tube detectors, providing 256 × 192 pixels. Data reduction followed standard procedures, as implemented in the Mantid software package.[74] The scattering data were corrected for wavelength-dependent sample transmission, for detector counting efficiency, and for instrument background on a pixel-to-pixel basis. The reduced scattered intensity was then azimuthally averaged. We converted the scattering intensities to absolute units of reciprocal centimeters (cm^{-1}) using a scale factor determined by measuring a porous SiO_2 powder standard.[75] After subtracting the scattering contribution of the empty quartz cell from that of the sample, the values of incoherent scattering intensity, I_{inc}, in samples no. 1 to 5 were

experimentally evaluated by neutron polarization analysis (see Table S1) with a neutron spin-echo spectrometer[76,77] installed at NG5, National Institute of Standards and Technology Center for Neutron Research, USA. Details and the importance of this technique were described previously.[48] The constant value I_{inc} was then subtracted from the net absolute intensity. The corrected scattered intensity distribution is treated as $I_{obs}(q)$. Since the values of ϕ_{HNO3}, ϕ_{H2O}, and ϕ_{TBP} in sample no. 1 are close to those of samples no. 2 to 5 (Table 1), the contribution of the HNO_3-H_2O-TBP aggregate to small-angle scattering was contained in $I_{obs}(q)$ of all sample solutions with the same level as sample no. 1. Therefore, $I_{sub}(q)$ originating from the contribution of small-angle scattering due to extracted $Zr(NO_3)_4(TBP)_2$ only in the organic phase was defined as $I_{sub}(q) = I_{obs}(q) - (1\text{-}\phi_{Zr(NO3)4(TBP)2}) \cdot I_{obs,no.1}(q)$, where $I_{obs,no.1}(q)$ is the $I_{obs}(q)$ of sample no. 1. The sample solutions were sealed in quartz cells with 2.0 mm sample thickness. All SANS data were acquired at 20 °C.

Computational methods. The structure of an isolated $Zr(NO_3)_4(TBP)_2$ complex was determined by an *ab initio* calculation, using the Gaussian09 software package[78] with the hybrid DFT functional B3LYP[79,80] implemented in the LanL2DZ basis for Zr,[81,82] and the 6-31G(d,p) basis for hydrogen, nitrogen, carbon, oxygen, and phosphorous. Geometry optimization of $Zr(NO_3)_4(TBP)_2$ in the organic phase was conducted by DFT calculation, where the crystal structure of a complex similar to $Zr(NO_3)_4(TBP)_2$, $Ce(NO_3)_4(OP(C_6H_5)_3)_2$,[83] was used as the initial input by replacing Ce with Zr. Additionally, all phenyl groups were replaced with butoxy groups. The polarizable continuum model (PCM)[84] was used to mimic the effect of the solvent

in this calculation, where the *n*-octane dielectric constant of 1.92[85] was used. The positions of the atoms in the optimized coordination structure were used as the initial structure to reproduce the EXAFS data and to calculate the scattering intensity distribution of the form factor of $Zr(NO_3)_4(TBP)_2$, based on the Debye scattering formula.[50,51]

For the MD simulations, the $Zr(NO_3)_4(TBP)_2$ complex was treated as a large molecule that cannot dissociate. The structure of the complex was that given above. To obtain the partial charges on each atom of the complex, single-point DFT calculations were performed using the optimized coordination structure as described above, but using the PCM for solvents with relative dielectric constants of 8.1781[86], 1.92406[78], and 78.3553[86]. These correspond to the dielectric constants of TBP, *n*-octane, and water, respectively.[86] The solvent cavities in the single-point calculations were built by using a series of overlapping atom-centered spheres with radii taken from the universal force field.[87] The DFT charge sets were obtained by fitting to an electrostatic potential calculated at various points around the molecule, generated according to the Merz-Singh-Kollman scheme.[88] Three different charge sets, which are denoted as the "TBP", "octane" and "water" charge sets, were obtained for the dielectric constants of TBP, *n*-octane, and water, respectively. The average value of the three DFT charge sets, which is denoted as the "average" charge set, was used as the partial charges for our $Zr(NO_3)_4(TBP)_2$ model. The details of the three DFT charge sets, which are in a GROMACS input file[89], are available in section no. 12 of this Supporting Information file. The rationale for this procedure is identical to that used for the determination of the TBP partial charges.[90] In addition, the effects of the four charge sets on the simulation results were examined and, as shown in Figure

S1, no statistically significant differences were found on distribution of cluster sizes. This is due to the fact that the partial charges vary by less than 1% between charge sets. In the organic phase, the complex can come into contact with a variety of polar and non-polar molecules and the charge set chosen must be a compromise that can model the interaction of a complex with a variety of neighboring molecules, some polar and some non-polar.

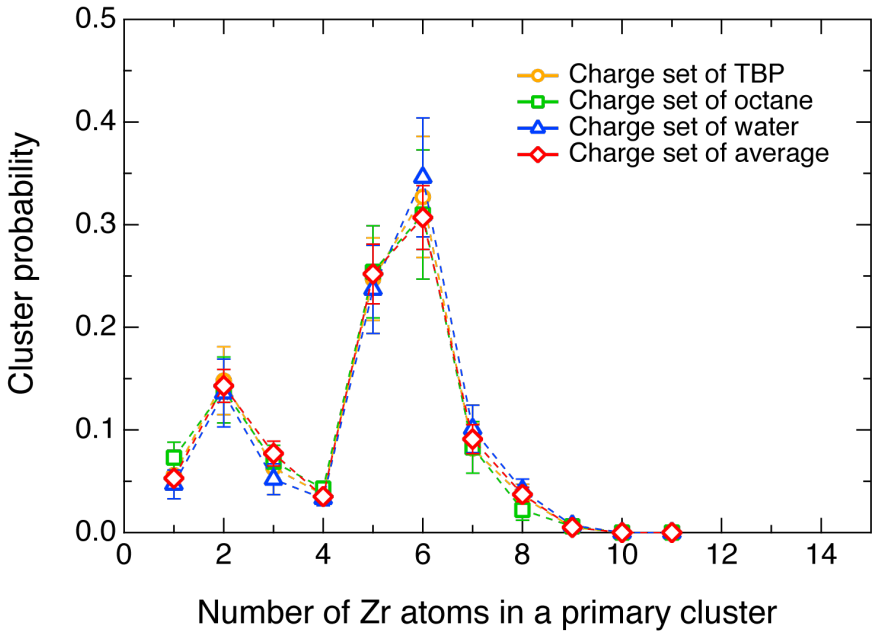

Figure S1. The size distribution function for primary clusters in sample no. 5. The bottom axis gives the number of Zr atoms in a primary cluster, while the vertical axis gives the number of primary clusters of that size divided by the total number of clusters. The simulation results of MD using the "TBP", "octane", "water" and "average" charge sets are shown as orange circles, green squares, blue triangles and red diamond, respectively.

To check if the simulation has reached equilibrium, we ran ten independent MD simulations, starting from random initial configurations. The results, which are shown in Figure S2, indicate that the cluster size distribution is identical, to within statistical uncertainty, for all ten systems.

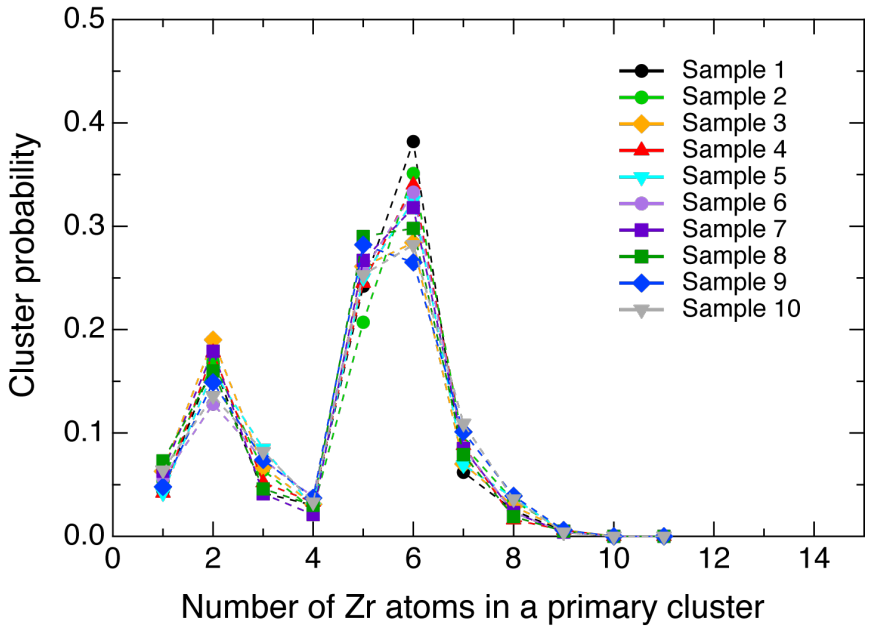

Figure S2. The size distribution function for primary clusters in sample no. 5. The bottom axis gives the number of Zr atoms in a primary cluster, while the vertical axis gives the number of primary clusters of that size divided by the total number of clusters. The data comes from ten independent MD simulations, each simulation starting from a random initial configuration. Error bars are omitted.

We now return to the DFT calculation of the geometry of the $Zr(NO_3)_4(TBP)_2$, for it is important to check how the final result depends on the starting configuration. Using the originally optimized $Zr(NO_3)_4(TBP)_2$ as an initial structure, the ligand coordination environment of the complex was investigated by exchanging the position of one of the TBP ligands for each of the nitrate ligands and re-optimizing the structure. Thus, five stereoisomers of the $Zr(NO_3)_4(TBP)_2$ were investigated in total. The five optimized $Zr(NO_3)_4(TBP)_2$ complexes differ in energy by no more than 11.0 kJ mol^{-1}. The different ligand coordination environment can be defined by the O_{TBP}-Zr-O_{TBP} angle; two of the complexes have angles of ~140° and three have angles of ~80°. The most stable complex with a O_{TBP}-Zr-O_{TBP} angle of ~140° was found to be only slightly lower in energy (1.0 kJ mol^{-1}) than the most stable complex with a O_{TBP}-Zr-O_{TBP} angle ~80°. Finally, starting from the originally optimized complex, one of the TBP molecules was rotated about its P=O bond by 60° and 120° and re-optimized; local energy minima were observed with complexes which differed in energy by no more than 6.8 kJ mol^{-1} from the originally optimized complex. The calculated SANS profiles based on the optimized complexes having an O_{TBP}-Zr-O_{TBP} angle of ~140° using Debye scattering formula for randomly orientated objects[50,51] agree with that experimentally obtained at $q > 4.0$ nm^{-1}. On the other hand, in the case of an O_{TBP}-Zr-O_{TBP} angle of ~80°, the calculated SANS profiles tend to deviate from the experimentally obtained one at $q > 4.0$ nm^{-1}. Therefore, the coordination species with an O_{TBP}-Zr-O_{TBP} angle of ~140° (Figure 2a) is probably a major component in the organic phase and we therefore used this structure, which is the same as that discussed earlier, in our simulation studies.

To complete the model, harmonic bonding and bending potentials of interactions were used to fix the length between the Zr cation and the coordinated oxygen atoms and their corresponding angles. The bond lengths and angles used were taken from the optimized structure from the DFT calculations. The force constant for bond length and angles were the same as the bond parameters for uranyl provided by Guilbaud and Wipff.[91] Full details of the force field, which is in the form of a GROMACS input file[89], are available. To elucidate the microscopic structure of the organic phases of the Zr−HNO_3/TBP−octane extraction systems, MD simulations were performed on systems with compositions close to those of the organic phases given in Table 1. For the MD simulations, the new atomistic model of $Zr(NO_3)_4(TBP)_2$ was used to represent the Zr complex. The Lennard–Jones parameters for Zr were taken from Li et al.[92] and the force field parameters for nitrates were taken from Sambasivarao and Acevedo.[93] The remaining force field potentials of interaction and details of the all-atom TBP model are given in our previous publication.[90] The *n*-octane model was taken from the OPLS-2005 force field[94] and the TIP3P model was used for H_2O because it was optimized for use with optimized potentials for liquid simulations (OPLS) force fields.[95] HNO_3 in our system was treated as an undissociated molecule, based on the assumption that the dissociation constant of HNO_3 is small in an organic environment. The force field parameters for HNO_3 were taken from Price et al.[96] The all-atom molecular models used here showed good accuracy in describing the structural properties of the HNO_3−H_2O/TBP−alkane systems and they reproduced the experimental small-angle X-ray scattering (SAXS) data collected from these

systems well.[44] Following the OPLS procedures, geometric combining rules were used to obtain the interactions of unlike pairs.

For all the MD simulations, we used cubic periodic boundary conditions. The Leapfrog algorithm[97] was used to integrate the equations of motion, where the time step was 1 fs. We applied a 1.2 nm cut-off to both the short-range Coulomb and Lennard–Jones interactions, where the potential switch functions[98] were applied from 0.9 nm to 1.2 nm to conserve the energies at the cut-off. For the long-range electrostatic potential, the particle mesh Ewald method was applied.[99] The isothermal-isobaric ensemble was used in these MD simulations, where the pressure and temperature were set as 1 bar and 20 °C, respectively. For each system considered, an equilibrated structure was obtained from the starting configuration using the velocity-rescaling thermostat[100] and the Berendsen barostat[101], where the simulations were run for 20 ns. The Nosé–Hoover thermostat[102,103] and Parrinello–Rahman barostat[104] were applied in the subsequent production runs, during which the simulation results were generated. The time constant used for the Nosé–Hoover thermostat and Parrinello–Rahman barostat were 0.2 ps and 5.0 ps, respectively. The production runs were 30 ns in length. Each of the simulated systems, which contained about 0.8 million atoms in total, had a box-length of approximately 20 nm. The corresponding number of Zr complexes that were simulated in systems no. 1 to 5 were 0, 32, 80, 120 and 160, respectively.

Hydrogen bonding analysis was performed to investigate the relation between the number of hydrogen bonds and the size of the primary clusters in our simulated systems. In the hydrogen bonding analysis, the hydrogen bonds between NO_3^-, HNO_3 or H_2O were considered and

counted. The criterion for determining the presence of a hydrogen bond is that the donor-acceptor distance should be no more than 0.35 nm and the acceptor-donor-hydrogen angle should be no more than 30°. The oxygen atoms that have covalent bonds with the hydrogen atoms in the H_2O and HNO_3 molecules were regarded as potential donors and the electronegative atoms that possess a lone electron pair were regarded as potential acceptors. For the hydrogen bonding analysis, we considered stable primary clusters, taken from system no. 5, with a range of aggregation numbers. By stable, we take the operational definition that the lifetime of the complex was more than 1 ns. Stable primary clusters consisting of 1, 2, 3, 5, and 6 were identified and indexed for hydrogen bonding analysis. The lifetime of a tetramer is less than 1 ns. The average number of hydrogen bonds per Zr atom was calculated for each cluster size. The results are shown in Figure 6a in the manuscript.

To examine the effect of the strength of the electrostatic interactions on the stability of primary clusters, we carried out five separate MD simulations on a stable primary cluster of six Zr complexes, taken from system no. 5. The partial charges on all atoms were scaled to 100%, 75%, 50%, 25%, and 0% of the original partial charges. By decreasing the partial charges the strength of the electrostatic interactions within the system decreases accordingly. The initial configuration of the five separate simulations were prepared in two steps as follows. Firstly, the stable primary cluster, which consists of 6 Zr complexes in system no. 5, was extracted and put into the center of a new, empty cubic simulation box with a dimension of 6 nm. Secondly, the empty space of the new simulation box was filled up with *n*-octane molecules to solvate the primary cluster. The five separate MD simulations, which started with the same initial

configuration stated above, were then simulated for 30 ns using the same simulation protocols described above. The final configurations of the systems using the 50% scaled and the original partial charges are shown in Figures S3a and b, respectively. It is clear that while the electrostatic strength of the original partial charges can hold the cluster together for 30 ns, the electrostatic strength of the 50% scaled partial charges is not enough to keep the cluster in its initial form and, as a result, the cluster consisting of 6 Zr complexes breaks up into three smaller clusters. This indicates that the electrostatic interactions, including short-range and long-range Coulomb forces and hydrogen bonds, are essential to keep the large primary clusters stable.

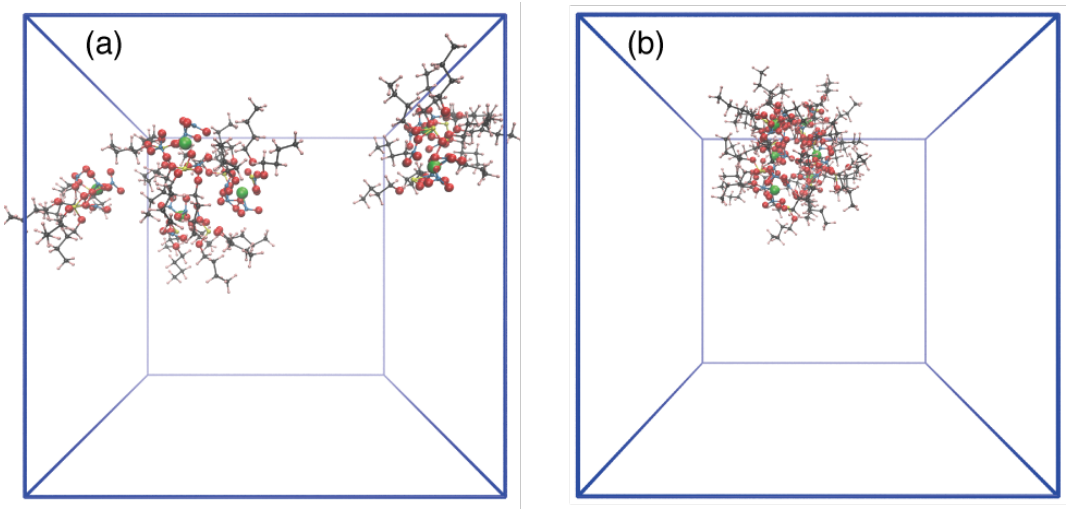

Figure S3. The final configurations of the MD simulations which started with a primary cluster consisting Zr complexes using (a) 50% scaled partial charges and (b) full scale partial charges.

To analyze the exposed hydrophilic area of the primary clusters to *n*-octane molecules, we calculated the Zr-C atom-atom radial distribution function, $g(r_{Zr\text{-}C})$, where C represents the carbon atoms in *n*-octane molecules. Note that the carbon atoms in TBP are not included in this analysis. The corresponding coordination numbers of Zr with C, $CN(r_{Zr\text{-}C})$, were also calculated. In this work, primary clusters consisting of 2, 3 and 6 Zr complexes were used to calculate $g(r_{Zr\text{-}C})$ and $CN(r_{Zr\text{-}C})$, respectively, which are shown for system no. 5 in Figures S4a and b.

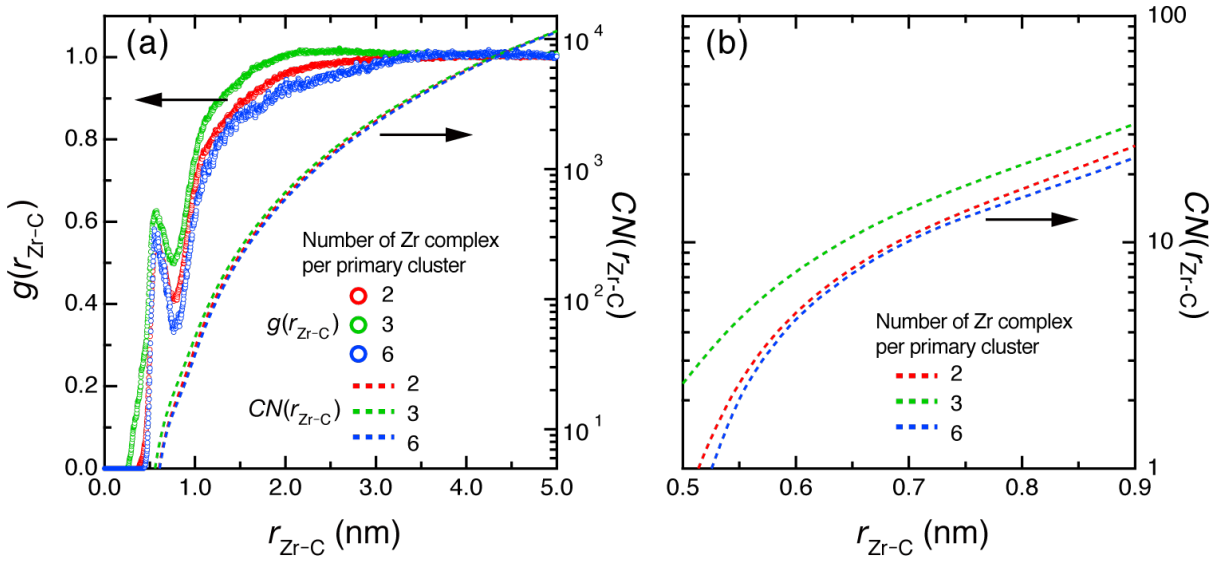

Figure S4. (a) Zr-C radial distribution function, $g(r_{Zr\text{-}C})$ (open circles), and corresponding coordination number of Zr with C, $CN(r_{Zr\text{-}C})$ (dashed lines). (b) Partial enlarged view of the $CN(r_{Zr\text{-}C})$ in the range of $r_{Zr\text{-}C}$ between 0.5 and 0.9 nm.

In Figure S4a, $g(r_{Zr\text{-}C})$ shows the average distribution of C atoms in *n*-octane around the Zr ions which belongs to a certain primary cluster, while $CN(r_{Zr\text{-}C})$ illustrates the corresponding coordination number of C around the Zr ions in that primary cluster. It is clear that $g(r_{Zr\text{-}C})$ for all three cluster sizes shows a small peak around 0.59 nm and a minimum around 0.78 nm. To gve a sense of scale, we note that the average distance between Zr ions and the coordinated oxygen atoms is about 0.23 nm while the average distance between Zr ions and the nitrogen atoms in the coordinated nitrates is around 0.4 nm. Hence, the C atoms in *n*-octane that are within a 0.78 nm range of a Zr ion are regarded as being in direct contact with the nitrates of the Zr complexes. In other words, the exposed hydrophilic area of the Zr complexes is related to the coordination number of C around Zr within a 0.78 nm radius. The magnified view of $CN(r_{Zr\text{-}C})$, within a range of 0.5 to 0.9 nm, is shown in Figure S4b. One can see that the $CN(r_{Zr\text{-}C})$ of the primary cluster consisting of 3 Zr complexes is larger than that of the primary cluster consisting of 2 or 6 Zr complexes. More specifically, the $CN(r_{Zr\text{-}C})$ are 15.9, 19.7 and 14.6 for the primary cluster consisting of 2, 3 and 6 Zr complexes, respectively. Hence, the exposed hydrophilic area of the Zr complexes consisting of 3 Zr complexes is the largest among the three cluster sizes. This level of unfavorable contact between polar and non-polar groups correlates with the fact that the trimer is the least stable cluster of the three, as is seen from the cluster analysis results shown in Figures 4b and S2.

2. Chemical structure of tri-*n*-butyl phosphate (TBP)

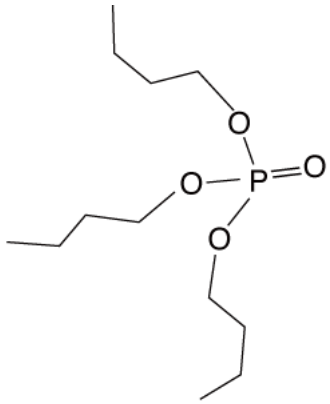

Figure S5. TBP chemical structure.

3. Concentration ratios of $[HNO_3]_{org,eq}/[Zr(NO_3)_4(TBP)_2]_{org,eq}$, $[H_2O]_{org,eq}/[Zr(NO_3)_4(TBP)_2]_{org,eq}$, and $[HNO_3]_{org,eq}/[H_2O]_{org,eq}$ in the organic, equilibrium (org,eq) phases

Table S1. Summary of the concentration ratios for $[HNO_3]_{org,eq}/[Zr(NO_3)_4(TBP)_2]_{org,eq}$, $[H_2O]_{org,eq}/[Zr(NO_3)_4(TBP)_2]_{org,eq}$, and $[HNO_3]_{org,eq}/[H_2O]_{org,eq}$ for sample nos. 1 to 5.

Sample no.	$[HNO_3]_{org,eq}$ / $[Zr(NO_3)_4(TBP)_2]_{org,eq}$	$[H_2O]_{org,eq}$ / $[Zr(NO_3)_4(TBP)_2]_{org,eq}$	$[HNO_3]_{org,eq}$ / $[H_2O]_{org,eq}$
1	–	–	6.2
2	40	7.3	5.5
3	20	3.8	5.3
4	11	3.2	3.6
5	9.4	2.3	4.1

4. EXAFS data for the third phase

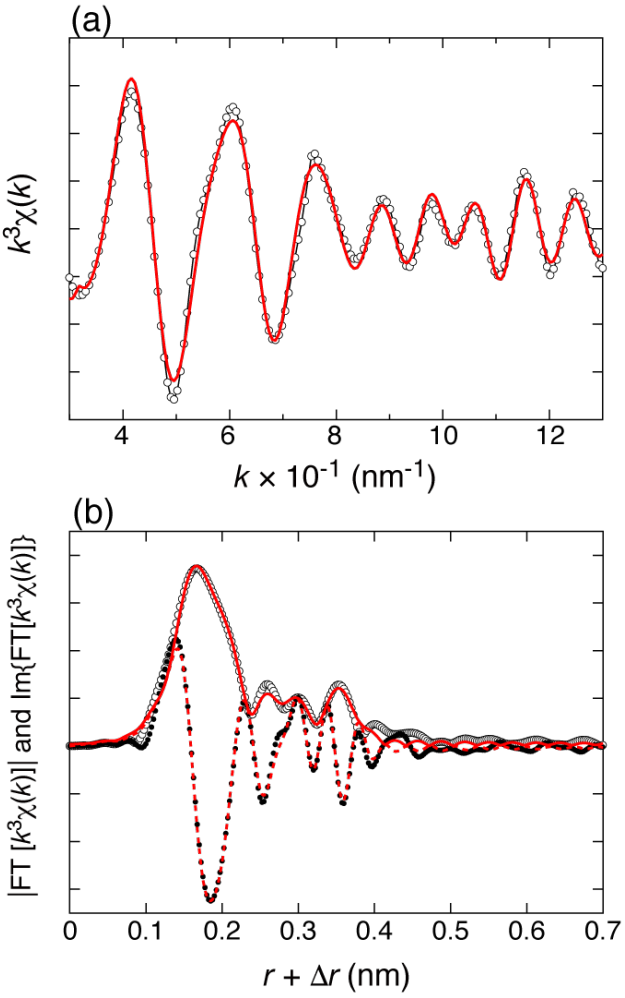

Figure S6. (a) k^3-weighted Zr K-edge EXAFS function, $k^3\chi(k)$ (open circles), (b) its corresponding Fourier transformation, |FT[$k^3\chi(k)$]| (open circles), and the imaginary part of FT[$k^3\chi(k)$], Im{FT[$k^3\chi(k)$]} (filled circles), obtained for the third phase upon solvent extraction of $Zr(NO_3)_4$–HNO_3/TBP–*n*-octane-d_{18}. The initial concentrations of $Zr(NO_3)_4$, HNO_3, and TBP in the extract are 0.376, 10.5, and 0.5 M, respectively. Red solid curves in (a) and (b) are the simulated $k^3\chi(k)$ and |FT[$k^3\chi(k)$]|, respectively, obtained using FEFF ver. 8.4 code and an optimized coordination structure of $Zr(NO_3)_4(TBP)_2$, determined by DFT calculation, as initial input. Similarly, the dashed red line in (b) shows the simulated Im{FT[$k^3\chi(k)$]}.

5. Guinier plots for evaluating the size of the high-order structure and $I_{sub}(q = 0)$

We carried out an analysis of $I_{sub}(q)$ to roughly evaluate the size of the high-order structure formed by $Zr(NO_3)_4(TBP)_2$ in the organic phase by applying Guinier's law,[55]

$$\ln I_{sub}(q) = \ln I_{sub}(q = 0) - \frac{1}{3} R_g^2 q^2 . \qquad \text{(S1)}$$

Figure S7 shows Guinier plots for samples no. 2 to 5, where the plot, $\ln I_{sub}(q)$ versus q^2, shows a linear relationship for $q < 1/R_g$, enabling R_g and $I_{sub}(q = 0)$ to be estimated from the slopes and intercepts of the lines. The solid lines in Figure S7 are the best-fit lines to eq S1. The evaluated R_g and $I_{sub}(q = 0)$ values of samples no. 2 to 5 were shown in main text of the manuscript.

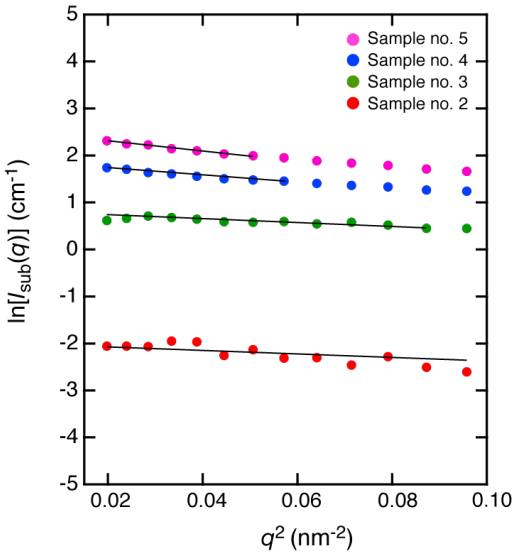

Figure S7. $\ln I_{sub}(q)$ plotted as a function of q^2 in accordance with eq S1. The solid black lines show the best-fit theoretical lines from Guinier's law for $q < 1/R_g$.

6. Theoretical modeling of the hierarchical aggregates

In this study, we construct theoretical models to interpret the experimental SANS data quantitatively. In the static approximation, the coherent scattering intensity distribution per unit volume, $I(q)$, is given by

$$I(q) = \frac{1}{V}\left\langle \sum_i \sum_j b_i b_j \exp\left(-i\vec{q}\cdot\vec{r_{ij}}\right)\right\rangle, \quad \text{(S2)}$$

where $\vec{r}_{ij} = \vec{r}_i - \vec{r}_j$ ($\vec{r}_i$ is the vector pointing of the ith element), V is the volume of the scatterer, and b_i is the scattering length of the ith element.[55] The angular bracket in eq S2 denotes an ensemble average of orientation of the scatterers.

In this study, the system consists of $Zr(NO_3)_4(TBP)_2$ complexes as solutes and a mixture of extracted HNO_3, extracted H_2O, uncoordinated TBP, and *n*-octane-d_{18} (diluent) as the matrix. Therefore, eq S2 can be further derived as

$$I(q) = n_{\text{complex}}\left[\left\langle |F(q)|^2\right\rangle + \left\langle |F(q)|\right\rangle^2 \{S(q)-1\}\right], \quad \text{(S3)}$$

where n_{complex} is the number density of the extracted $Zr(NO_3)_4(TBP)_2$ complex, $F(q)$ is the scattering amplitude of the complex, and $S(q)$ is the structure factor of the complex.[105] n_{complex} can be calculated as $n_{\text{complex}} = \phi_{Zr(NO3)4(TBP)2} \cdot d_{Zr(NO3)4(TBP)2} \cdot N_A / M_{Zr(NO3)4(TBP)2}$, where N_A and $M_{Zr(NO3)4(TBP)2}$ are Avogadro's number and the molecular weight of $Zr(NO_3)_4(TBP)_2$, respectively. The values of n_{complex} in samples no. 2 to 5 are listed in Table S2.

Table S2. Summary of parameters in relation to the SANS profile analyses of the organic phases.

Sample no.	$n_{complex}$ (cm^{-3})	ρ_s (cm^{-2})	I_{inc} (cm^{-1})[a]
1	–[b]	–[b]	0.122 ± 0.005
2	0.386×10^{19}	5.570×10^{10}	0.119 ± 0.004
3	1.002×10^{19}	5.571×10^{10}	0.123 ± 0.004
4	1.465×10^{19}	5.572×10^{10}	0.124 ± 0.005
5	1.928×10^{19}	5.612×10^{10}	0.116 ± 0.005

[a]Error represents ±1 standard deviation throughout the paper.
[b]Sample no. 1 does not contain extracted $[Zr(NO_3)_4(TBP)_2]_{org}$ because $[Zr(NO_3)_4]_{aq} = 0$ (Table 1).

The scattering amplitude represents the positions of the nuclei in an individual complex with the corresponding scattering length densities as weighting factors as

$$F(q) = \sum_k v_k f_k(q) \Delta\rho_k \exp\left(-i\vec{q}\cdot\vec{X_k}\right), \qquad \text{(S4)}$$

where v_k is the excluded volume of the kth atom, $\Delta\rho_k$ is the difference between the scattering length density of the kth nucleus and that of the matrix, $f_k(q)$ is the atomic scattering factor of the kth atom, and $\vec{X}_k$ is the vector pointing from the center of mass of a single complex to the position of the kth nucleus. The scattering length density of the kth nucleus, ρ_k, is defined as ρ_k

= b_k/v_k, so that $\Delta\rho_k$ is given by $\Delta\rho_k = \rho_k - \rho_s$. ρ_s (see Table S1) is the scattering length density of the matrix, which is given by

$$\rho_S = (\phi_{\mathrm{TBP}}\rho_{\mathrm{TBP}} + \phi_{\mathrm{HNO3}}\rho_{\mathrm{HNO3}} + \phi_{\mathrm{H2O}}\rho_{\mathrm{H2O}} + \phi_{n\text{-octane-}d18}\rho_{n\text{-octane-}d18}) / \phi_{\mathrm{matrix}}, \quad \text{(S5)}$$

where ρ_{TBP}, ρ_{HNO3}, ρ_{H2O}, and $\rho_{n\text{-octane-}d18}$ are the scattering length densities of TBP, HNO_3, H_2O, and *n*-octane-d_{18}, respectively, and ϕ_{matrix} is equal to the sum of the volume fractions of the matrix components, that is, $\phi_{\mathrm{matrix}} = \phi_{\mathrm{HNO3}} + \phi_{\mathrm{H2O}} + \phi_{\mathrm{TBP}} + \phi_{\mathrm{Octane}\text{-}d18}$. According to the Debye scattering formula for randomly orientated objects,[50,51] the ensemble average of the scattering amplitude, $\langle F(q)\rangle$, and that of its square, $\langle |F(q)|^2\rangle$, are derived as

$$\left\langle F(q)\right\rangle = \sum_k v_k f_k(q)\Delta\rho_k \frac{\sin\left(q\bar{X}_k\right)}{q\bar{X}_k} \quad \text{(S6)}$$

and

$$\left\langle \left|F(q)\right|^2 \right\rangle = \sum_k \sum_l v_k v_l f_k(q) f_l(q)\Delta\rho_k\Delta\rho_l \frac{\sin\left(q\bar{r}_{kl}\right)}{q\bar{r}_{kl}}, \quad \text{(S7)}$$

with $\bar{X}_k$ being the distance between the center of mass and the *k*th nucleus and $\bar{r}_{kl}$ being the distance between the *k*th and *l*th nuclei. The atomic scattering factors for X-ray diffraction are reflected by the electron orbitals of the atoms and are typically approximated by a sum of

Gaussians.[106] However, the atomic scattering factors for neutron scattering are affected by the probability of the nuclei. By choosing a Gaussian distribution function, $g(r) \propto \exp(-r^2/2\sigma_p^2)$,[107] $f_k(q)$ is given by

$$f_k(q) = \frac{4\pi}{v_k}\int_0^\infty r^2 \exp\left\{-\frac{r^2}{2\sigma_p^2}\right\}\frac{\sin(qr)}{qr}dr = \exp\left(-q^2\sigma_p^2/2\right), \quad \text{(S8)}$$

with

$$v_k = 4\pi\int_0^\infty r^2 \exp\left(-\frac{r^2}{2\sigma_p^2}\right)dr = 2\pi\sqrt{2\pi}\sigma_p^3 . \quad \text{(S9)}$$

The structure factor $S(q)$ reflects the inter-particle interaction. In this system, a cluster of $Zr(NO_3)_4(TBP)_2$ complexes is considered; that is, the N complexes distribute spherically and randomly around the center complex at a distance R_S (see Figures. 2a and b and Figure S8a). In this case, $S(q)$ is expressed as[49]

$$S(q,N,R) = 1 + \frac{1}{N}\left[2(N-1)\frac{\sin(qR)}{qR} + (N-1)(N-2)\left\{\frac{\sin(qR)}{qR}\right\}^2\right]. \quad \text{(S10)}$$

For small primary clusters consisting of N complexes with radius R_S forming a large aggregate (super-clusters) of M primary clusters with radius R_L (see Figure 2c and Figure S8b), the scattering intensity distribution is given based on eq S3 by

$$I(q) = n_{\text{large}}\left[\left\langle\left|F_{\text{cluster}}(q)\right|^2\right\rangle + \left\langle\left|F_{\text{cluster}}(q)\right|\right\rangle^2\left\{S(q,M,R_{\text{L}})-1\right\}\right] \tag{S11}$$

with

$$\left\langle\left|F_{\text{cluster}}(q)\right|^2\right\rangle = \left[\left\langle\left|F(q)\right|^2\right\rangle + \left\langle\left|F(q)\right|\right\rangle^2\left\{S(q,N,R_{\text{S}})-1\right\}\right] \tag{S12}$$

and

$$\left\langle\left|F_{\text{cluster}}(q)\right|\right\rangle = \left\langle\left|F(q)\right|\right\rangle\left[1+(N-1)\frac{\sin(qR_{\text{S}})}{qR_{\text{S}}}\right]. \tag{S13}$$

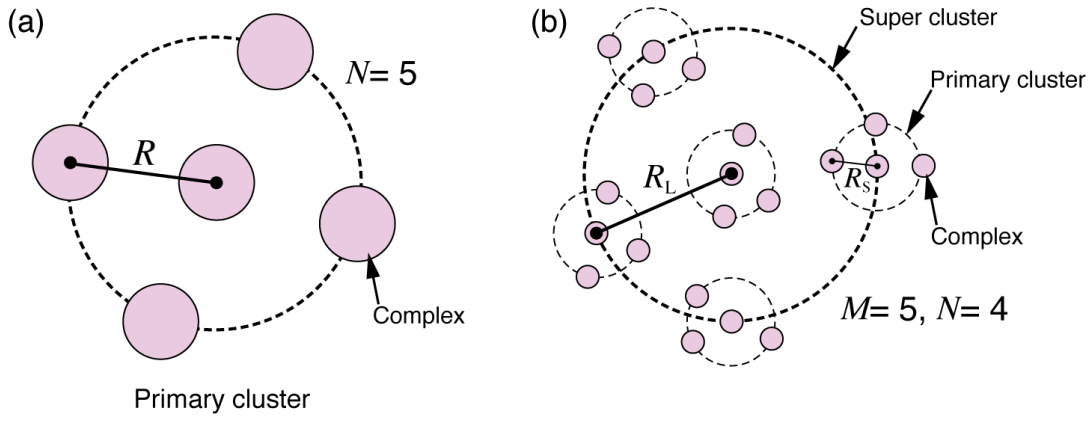

Figure S8. Schematic diagrams of the theoretical model used for analyzing SANS profiles. (a) A cluster in which the complexes distribute with radius R (N = 5) around the central particle, (b) primary clusters assemble into a super-cluster, where primary clusters with radius R_{S} surround the central cluster with radius R_{L} (M = 5 and N = 4 in the text).

The distributions of R_L and R_S were considered to reproduce the scattering intensity distribution precisely, and thus the Schultz distribution with the corresponding standard deviations, σ_L and σ_S, respectively, was used.[57]

7. Result of SANS data analysis using scattering theory with $M = 1$ for the organic solution of sample no. 5

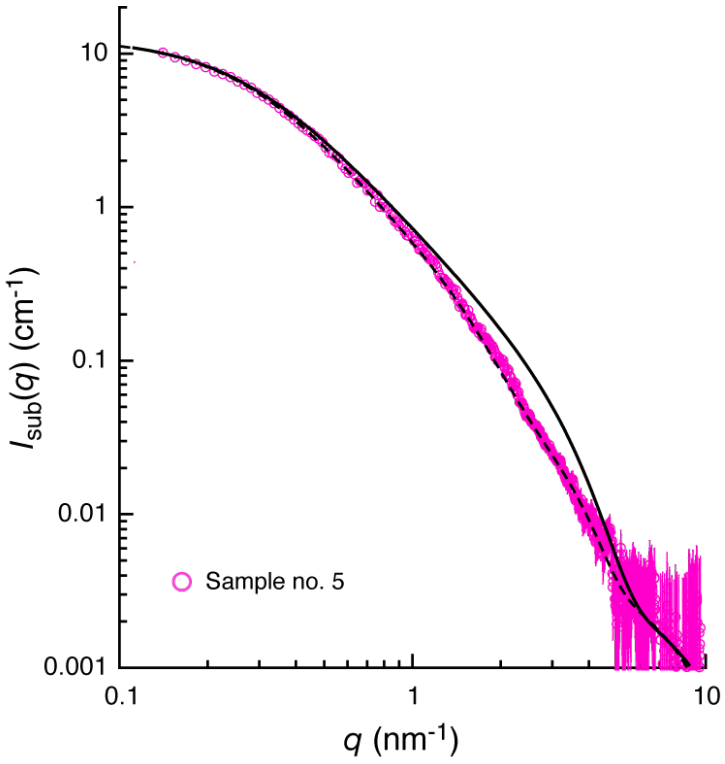

Figure S9. SANS profile obtained for sample no. 5 (pink open circles) and the best-fit curve (black solid line) using eqs S10 to S13 with M = 1 based on the scattering theory of the hierarchical aggregation model. The difference between the experimental data, $I_{sub}(q)$, and the best-fit theoretical scattering curves with the characteristic parameters $N = 171 \pm 4.3$, $R_S = 5.4 \pm 0.46$ nm, and $\sigma_S = 0.24 \pm 0.02$ nm is evident, particularly at 1.0 nm^{-1} < q < 5.0 nm^{-1}. Consequently, the calculated curve does not agree for $M = 1$ using reasonable fitting parameters. Dashed line is the best-fit curve shown in Figure 3b using eqs S10 to S13 and the characteristic parameters in Table 3. Error of the characteristic parameters in the fitting represents ±1 standard deviation.

8. Contribution to SANS intensity distribution of a primary cluster

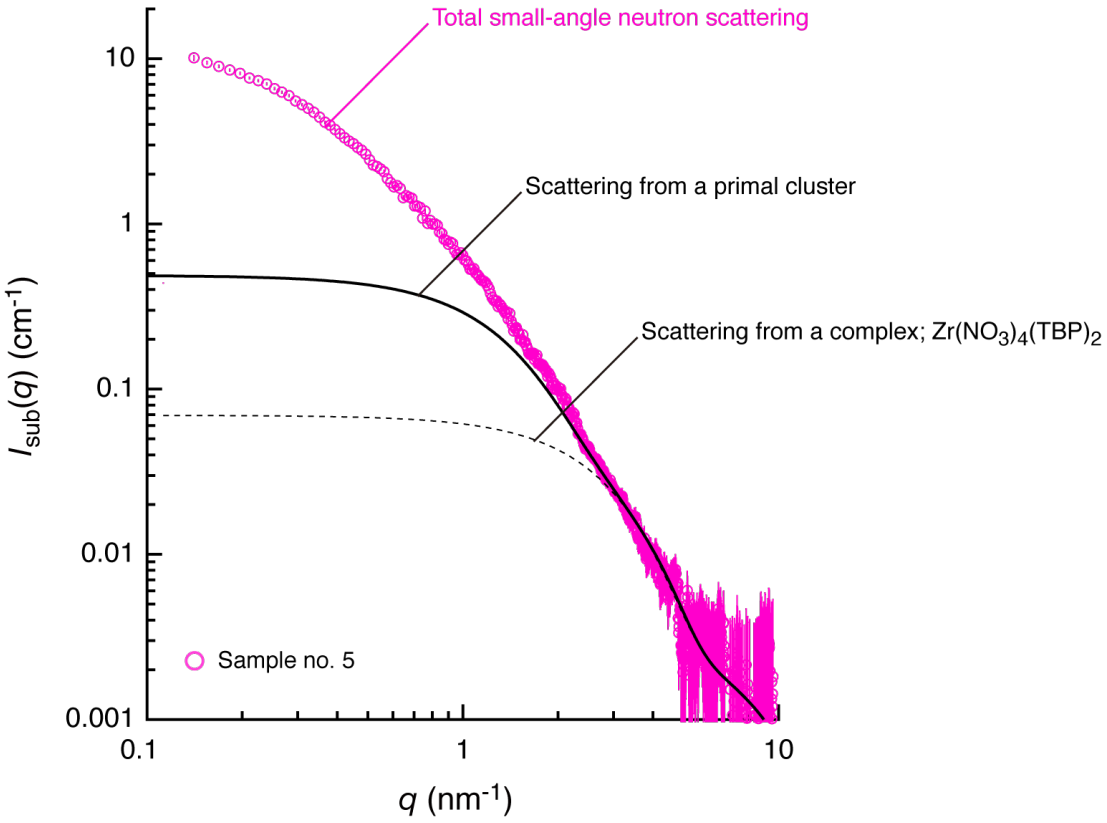

Figure S10. SANS profile obtained for sample no. 5 (pink open circles) and the contribution to the SANS intensity distribution of a primary cluster (black solid line) with the theoretical analysis using eqs S10 to S13 with $M = 1$. Black dashed line is the contribution to the SANS intensity distribution of $Zr(NO_3)_4(TBP)_2$ calculated with the Debye scattering formula.

9. Method of potentiometric titration to determine [HNO_3] in the aqueous phase

Potentiometric titration experiments were performed as follows. The sample solution was diluted 40-fold with an aqueous solution of 0.25 M ammonium oxalate. Ammonium oxalate was added to mask the zirconium ions. The diluted sample solutions were titrated with an aqueous solution containing 1 M NaOH using an automatic titrator to a pH of about 10. The equivalence points appeared at pH 6.0 to 6.7, and the HNO_3 concentration was calculated from the titration volume at the equivalence point. During titration, a white precipitation appeared around pH 9.8 and was likely zirconium hydroxide or an ammine complex resulting from the dissociation of ammonium ions. Given that no precipitate was observed below pH = 9.0 and that the equivalence points were at pH 6.0 to 7.7, this precipitate likely did not affect the determination of HNO_3 concentration.

10. EXAFS data and analysis for initial aqueous phase for preparing sample no. 5

The coordination structure of the zirconium complex in the initial aqueous phase of sample no. 5 was examined by EXAFS measurement as shown in Figure S11, where the data were analyzed by employing curve fitting with the simulation code FEFF ver. 8.4[54]. The structural parameters are shown in Table S3. As a result, it was clarified that $Zr(NO_3)_4(H_2O)$ is a major species in the initial aqueous phase at $[HNO_3]_{aq}$ = 10.5 M.

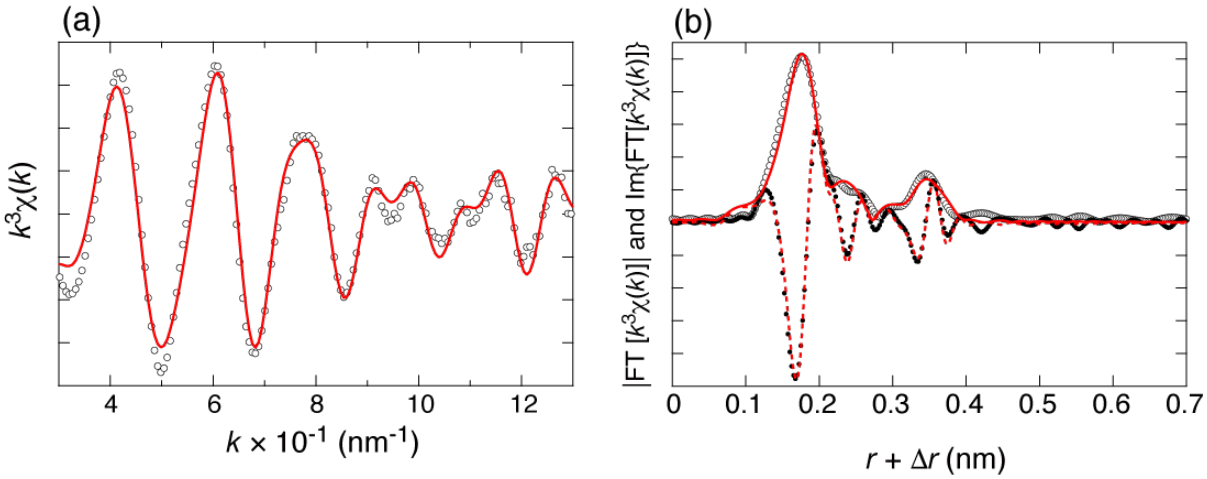

Figure S11. (a) k^3-weighted Zr K-edge EXAFS function, $k^3\chi(k)$, (open circles), (b) its corresponding Fourier transformation, |FT[$k^3\chi(k)$]|, (open circles), and the imaginary part of FT[$k^3\chi(k)$], Im{FT[$k^3\chi(k)$]} (filled circles), obtained for initial aqueous phase of sample no. 5. Red solid curves in (a) and (b) are the simulated $k^3\chi(k)$ and |FT[$k^3\chi(k)$]|, respectively, obtained using FEFF ver. 8.4 code and a single crystal structure of $Zr(NO_3)_3(H_2O)_3$ as initial input[108]. The dashed red line in (b) shows the simulated Im{FT[$k^3\chi(k)$]}.

Table S3. Structural parameters evaluated by fitting analysis of initial aqueous phase of sample no. 5.

Path	*CN*	r_{EXAFS} (nm)	σ_{DW}^2 (nm^2)	ΔE_0 (eV)	S_0^2
Zr-O	9.3	0.228	0.00008	4.07	0.9
Zr-N_{NO3}	4.0	0.275	0.00003	4.07	0.9
Zr-N-$O_{multiple}$	4.0	0.395	0.00002	4.07	0.9

Additionally, the $k^3\chi(k)$ and |FT[$k^3\chi(k)$]| obtained for the initial aqueous phase of sample no. 5 was compared with those obtained for a zirconyl nitrate complex in 3.0 M HNO_3 aqueous solution as shown in Figure S12. Note that this control sample is used to provide solid evidence of $Zr(NO_3)_4(H_2O)$ formation in the initial aqueous phase in the absence of the zirconyl nitrate complexes, where the solution was prepared by dissolving 50 mM of zirconyl nitrate dehydrate in 3.0 M HNO_3 aqueous solution. In Figure S12b, two distinct peaks were observed in the |FT[$k^3\chi(k)$]| of both $Zr(NO_3)_4(H_2O)$ and the zirconyl nitrate complex in aqueous solutions. However, the position of the weaker peak (second peak) obtained for $Zr(NO_3)_4(H_2O)$ is shorter $r + \Delta r$ than that obtained for zirconyl nitrate complexes, whereas the positions of the most intense peaks (first peak) in |FT[$k^3\chi(k)$]| agree with each other. The EXAFS data of zirconyl nitrate complex was analyzed according to the same manner described above. The structural parameters obtained are shown in Table S4. This result indicates that the zirconyl nitrate complexes form a multi-nuclear species due to Zr-O-Zr unit. In conclusion, it is clear that the zirconyl nitrate complex does not exist in the initial aqueous phase of our solvent extraction

systems. This is attributed to the very high HNO_3 concentration, i.e., $[HNO_3]_{aq,in}$ =10.5 M, in the aqueous phase.

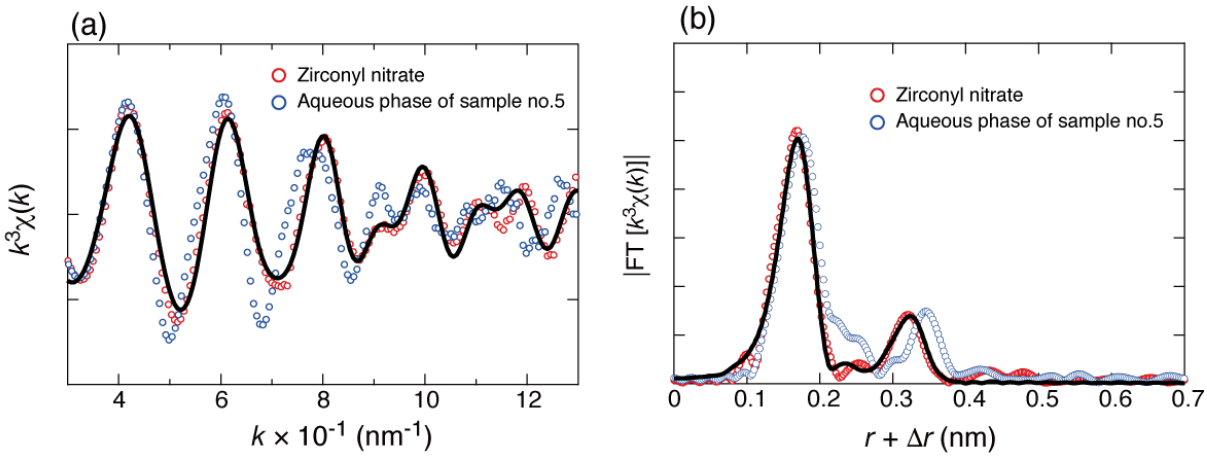

Figure S12. (a) k^3-weighted Zr K-edge EXAFS function, $k^3\chi(k)$, and (b) its corresponding Fourier transformation, |FT[$k^3\chi(k)$]|, obtained for the initial aqueous phase of sample no. 5 (red open circles) and zirconyl nitrate complex in 3.0 M HNO_3 aqueous solution (blue open circles). Black solid curves in (a) and (b) are the simulated $k^3\chi(k)$ and |FT[$k^3\chi(k)$]|, respectively, obtained for zirconyl nitrate complex using FEFF ver. 8.4 code.

Table S4. Structural parameters evaluated by fitting analysis of the zirconyl nitrate complex.

Path	*CN*	r_{EXAFS} (nm)	σ_{DW}^2 (nm^2)	ΔE_0 (eV)	S_0^2
Zr-O	8.3	0.218	0.00007	0.213	0.9
Zr-N_{NO3}	1.7	0.272	0.00004	0.213	0.9
Zr- Zr	2.0	0.358	0.00007	0.213	0.9
Zr-N-$O_{multiple}$	1.6	0.390	0.00010	0.213	0.9

11. Full references

(1) Gompper G.; Schick M. In *Phase Transitions and Critical Phenomena*; Domb, C. and Lebowitz, J., Ed.; Academic Press: London, 1994; Vol. 16, p1–176.

(2) Schwuger, M. J.; Stickdorn, K.; Schomacker, R. Microemulsions in technical processes. *Chem. Rev.* **1995,** *95*, 849–864.

(3) Winsor, P. A. *Solvent Properties of Amphiphilic Compounds*; Butterworths: London, 1954.

(4) Lindman, B.; Wennerström, H. Miceles. Amphiphile aggregation in aqueous solution. *Top. Curr. Chem.* **1980**, *87*, 1–83.

(5) Eicke, H.-F. Surfactants in nonpolar solvents. Aggregation and micellization. *Top. Curr. Chem.* **1980**, *87*, 85–145.

(6) Fischer, S.; Exner, A.; Zielske, K.; Perlich, J.; Deloudi, S.; Steurer, W.; Lindner, P.; Forster, S. Colloidal quasicrystals with 12-fold and 18-fold diffraction symmetry. *Proc. Natl. Acad. Sci. U. S. A.* **2011,** *108*, 1810–1814.

(7) Zemb, T. Flexibility, Persistence length and bicontinuous microstructures in microemulsions. *C. R. Chim.* **2009**, *12*, 218–224.

(8) Zemb, T.; Holmberg, K.; Kunz, W. Special topic: Weak self assembly. *Curr. Opin. Colloid Interface Sci.* **2016**, *22*, A1–A3.

(9) Zemb, T.; Kunz, W. Weak aggregation: State of the art, expectations and open questions. *Curr. Opin. Colloid Interface Sci.* **2016**, *22*, 113–119.

(10) Pini, D.; Parola, A. Pattern formation and self-assembly driven by competing interactions. *Soft Matter* **2017**, *13*, 9259–9272.

(11) Foffi, G.; De Michele, C.; Sciortino, F.; Tartaglia, P. Scaling of dynamics with the range of interaction in short-range attractive colloids. *Phys. Rev. Lett.* **2005**, *94*.

(12) Zaccarelli, E. Colloidal gels: equilibrium and non-equilibrium routes. *J. Phys.-Condes. Matter* **2007**, *19*, 323101.

(13) Bera, M. K.; Qiao, B. F.; Seifert, S.; Burton-Pye, B. P.; Olvera de la Cruz, M.; Antonio, M. R. Aggregation of heteropolyanions in aqueous solutions exhibiting short-range attractions and long-range repulsions. *J. Phys. Chem. C* **2016**, *120*, 1317–1327.

(14) Poon, W. C. K.; Haw, M. D. Mesoscopic structure formation in colloidal aggregation and gelation. *Adv. Colloid Interface Sci.* **1997**, *73*, 71–126.

(15) Lu, P. J.; Zaccarelli, E.; Ciulla, F.; Schofield, A. B.; Sciortino, F.; Weitz, D. A. Gelation of particles with short-range attraction. *Nature* **2008**, *453*, 499–505.

(16) Kim, S. A.; Jeong, K. J.; Yethiraj, A.; Mahanthappa, M. K. Low-symmetry sphere packings of simple surfactant micelles induced by ionic sphericity. *Proc. Natl. Acad. Sci. U. S. A.* **2017**, *114*, 4072–4077.

(17) Bauer, C.; Bauduin, P.; Dufreche, J. F.; Zemb, T.; Diat, O. Liquid/liquid metal extraction: Phase diagram topology resulting from molecular interactions between extractant, ion, oil and water. *Eur. Phys. J.-Spec. Top.* **2012**, *213*, 225–241.

(18) Erlinger, C.; Gazeau, D.; Zemb, T.; Madic, C.; Lefrancois, L.; Hebrant, M.; Tondre, C. Effect of nitric acid extraction on phase behavior, microstructure and interactions between primary aggregates in the system dimethyldibutyltetradecylmalonamide (DMDBTDMA) /

n-dodecane / water: A phase analysis and small angle X-ray scattering (SAXS) characterisation study. *Solvent Extr. Ion Exch.* **1998**, *16*, 707–738.

(19) Testard, F.; Zemb, T.; Bauduin, P.; Berthon, L. In *Ion Exchange and Solvent Extraction: A Series of Advances*; Moyer, B. A., Ed.; CRC Press: Boca Raton, 2010; Vol. 19, p381–428.

(20) Baxter, R. J. Percus-Yevick equation for hard spheres with surface adhesion. *J. Chem. Phys.* **1968**, *49*, 2770–2774.

(21) Schulz, W. W.; Navratil, J. D. *Science and Technology of Tributyl Phosphate.* CRC Press: Boca Raton, FL. 1984.

(22) Osseo-Asare, K. Aggregation, reversed micelles, and microemulsions in liquid-liquid extraction: the tri-*n*-butyl phosphate-diluent-water-electrolyte system. *Adv. Colloid Interface Sci.* **1991**, *37*, 123–173.

(23) Diss, R.; Wipff, G. Lanthanide cation extraction by malonamide ligands: from liquid-liquid interfaces to microemulsions. A molecular dynamics study. *Phys. Chem. Chem. Phys.* **2005**, *7*, 264–272.

(24) Jensen, M. P.; Yaita, T.; Chiarizia, R. Reverse-micelle formation in the partitioning of trivalent *f*-element cations by biphasic systems containing a tetraalkyldiglycolamide. *Langmuir* **2007**, *23*, 4765–4774.

(25) Guo, F. Q.; Li, H. F.; Zhang, Z. F.; Meng, S. L.; Li, D. Q. Reversed micelle formation in a model liquid-liquid extraction system. *J. Colloid Interface Sci.* **2008**, *322*, 605–610.

(26) Chiarizia, R.; Briand, A.; Jensen, M. P.; Thiyagarajan, P. SANS study of reverse micelles formed upon the extraction of inorganic acids by TBP in *n*-octane. *Solvent Extr. Ion Exch.* **2008**, *26*, 333–359.

(27) Ganguly, R.; Sharma, J. N.; Choudhury, N. TODGA based w/o microemulsion in dodecane: An insight into the micellar aggregation characteristics by dynamic light scattering and viscometry. *J. Colloid Interface Sci.* **2011**, *355*, 458–463.

(28) Ellis, R. J.; Meridiano, Y.; Chiarizia, R.; Berthon, L.; Muller, J.; Couston, L.; Antonio, M. R. Periodic behavior of lanthanide coordination within reverse micelles. *Chem. –Eur. J.* **2013**, *19*, 2663–2675.

(29) Guilbaud, P.; Zemb, T. Depletion of water-in-oil aggregates from poor solvents: Transition from weak aggregates towards reverse micelles. *Curr. Opin. Colloid Interface Sci.* **2015**, *20*, 71–77.

(30) Bley, M.; Siboulet, B.; Karmakar, A.; Zemb, T.; Dufreche, J. F. A predictive model of reverse micelles solubilizing water for solvent extraction. *J. Colloid Interface Sci.* **2016**, *479*, 106–114.

(31) Diamant, H.; Andelman, D. Free energy approach to micellization and aggregation: Equilibrium, metastability, and kinetics. *Curr. Opin. Colloid Interface Sci.* **2016**, *22*, 94–98.

(32) Gao, S.; Sun, T. X.; Chen, Q. D.; Shen, X. H. Characterization of reversed micelles formed in solvent extraction of thorium(IV) by bis(2-ethylhexyl) phosphoric acid. Transforming from rodlike to wormlike morphology.*Radiochim. Acta* **2016**, *104*, 457–469.

(33) Chen, Y. S.; Duvail, M.; Guilbaud, P.; Dufreche, J. F. Stability of reverse micelles in rare-earth separation: a chemical model based on a molecular approach. *Phys. Chem. Chem. Phys.* **2017**, *19*, 7094–7100.

(34) Tonova, K.; Lazarova, Z. Reversed micelle solvents as tools of enzyme purification and enzyme-catalyzed conversion. *Biotechnol. Adv.* **2008**, *26*, 516–532.

(35) Ballesteros-Gomez, A.; Sicilia, M. D.; Rubio, S. Supramolecular solvents in the extraction of organic compounds. A review. *Anal. Chim. Acta* **2010**, *677*, 108–130.

(36) Poirot, R.; Le Goff, X.; Diat, O.; Bourgeois, D.; Meyer, D. Metal recognition driven by weak interactions: A case study in solvent extraction. *ChemPhysChem* **2016**, *17*, 2112–2117.

(37) Prevost, S.; Gradzielski, M.; Zemb, T. Self-assembly, phase behaviour and structural behaviour as observed by scattering for classical and non-classical microemulsions. *Adv. Colloid Interface Sci.* **2017**, *247*, 374–396.

(38) Moyer, B. A. Ed. *Ion Exchange and Solvent Extraction: A Series of Advances.* CRC Press: Boca Raton, 2010, *19*.

(39) Ellis, R. J. Critical exponents for solvent extraction resolved using SAXS. *J. Phys. Chem. B* **2014**, *118*, 315–322.

(40) Plaue, J.; Gelis, A.; Czerwinski, K.; Thiyagarajan, P.; Chiarizia, R. Small-angle neutron scattering study of plutonium third phase formation in 30% TBP/HNO_3/alkane diluent systems. *Solvent Extr. Ion Exch.* **2006**, *24*, 283–298.

(41) Chiarizia, R.; Jensen, M. P.; Rickert, P. G.; Kolarik, Z.; Borkowski, M.; Thiyagarajan, P. Extraction of zirconium nitrate by TBP in *n*-octane: Influence of cation type on third phase formation according to the "sticky spheres" model. *Langmuir* **2004**, *20*, 10798–10808.

(42) Ivanov, P.; Mu, J.; Leay, L.; Chang, S. Y.; Sharrad, C. A.; Masters, A. J.; Schroeder, S. L. M. Organic and third phase in HNO_3/TBP/*n*-dodecane system: No reverse micelles. *Solvent Extr. Ion Exch.* **2017**, *35*, 251–265.

(43) Servis, M.; Wu, D.; Braley, J. Network analysis and percolation transition in hydrogen bonded clusters: nitric acid and water extracted by tributyl phosphate. *Phys. Chem. Chem. Phys.* **2017**, *19*, 11326–11339.

(44) Mu, J.; Motokawa, R.; Akutsu, K.; Nishitsuji, S.; Masters, A. J. A novel microemulsion phase transition: Toward the elucidation of third-phase formation in spent nuclear fuel reprocessing. *J. Phys. Chem. B*. **2018**, *122*, 1439–1452.

(45) Baldwin, A. G.; Servis, M. J.; Yang, Y.; Bridges, N. J.; Wu, D. T.; Shafer, J. C. The structure of tributyl phosphate solutions: Nitric acid, uranium (VI), and zirconium (IV). *J. Mol. Liq.* **2017**, *246*, 225–235.

(46) Borkowski, M.; Chiarizia, R.; Jensen, M. P.; Ferraro, J. R.; Thiyagarajan, P.; Littrell, K. C. SANS study of third phase formation in the Th(IV)-HNO3/TBP-*n*-octane system. *Sep. Sci. Technol.* **2003**, *38*, 3333–3351.

(47) Chiarizia, R.; Jensen, M. P.; Borkowski, M.; Ferraro, J. R.; Thiyagarajan, P.; Littrell, K. C. Third phase formation revisited: The U(VI), HNO_3-TBP, *n*-dodecane system. *Solvent Extr. Ion Exch.* **2003**, *21*, 1–27.

(48) Motokawa, R.; Endo, H.; Nagao, M.; Heller, W. T. Neutron polarization analysis for biphasic solvent extraction systems. *Solvent Extr. Ion Exch.* **2016**, *34*, 399–406.

(49) Koga, T.; Tanaka, F.; Motokawa, R.; Koizumi, S.; Winnik, F. M. Theoretical modeling of associated structures in aqueous solutions of hydrophobically modified telechelic PNIPAM based on a neutron scattering study. *Macromolecules* **2008**, *41*, 9413–9422.

(50) Debye, P. Zerstreuung von röntgenstrahlen. *Ann. Phys. (Berlin, Ger.)* **1915**, *351*, 809–823.

(51) Svergun, D.; Barberato, C.; Koch, M. H. J. *J.* CRYSOL– a program to evaluate X-ray solution scattering of biological macromolecules from atomic coordinates. *Appl. Crystallogr.* **1995**, *28*, 768–773.

(52) Antonio, M. R.; Demars, T. J.; Audras, M.; Ellis, R. J. Third phase inversion, red oil formation, and multinuclear speciation of tetravalent cerium in the tri-*n*-butyl phosphate-*n*-dodecane solvent extraction system. *Sep. Sci. Technol.* **2018,** *53*, 1834–1847.

(53) Antonio, M. R.; Ellis, R. J.; Estes, S. L.; Bera, M. K. Structural insights into the multinuclear speciation of tetravalent cerium in the tri-*n*-butyl phosphate-*n*-dodecane solvent extraction system. *Phys*. *Chem*. *Chem*. *Phys*. **2017,** *19*, 21304–21316.

(54) Ankudinov, A. L.; Ravel, B.; Rehr, J. J.; Conradson, S. D. Real-space multiple-scattering calculation and interpretation of X-ray-absorption near-edge structure. *Phys. Rev. B* **1998,** *58*, 7565–7576.

(55) Roe, R.-J.. *Methods of X-ray and Neutron Scattering in Polymer Science*, 1st ed.; Oxford University Press: NY, 2000.

(56) Okuhara, T.; Mizuno, N.; Misono, M. In *Adv. Catal.*; Eley, D. D., Haag, W. O., Gates, B., Eds. 1996; Vol. 41, 113–252.

(57) Bartlett, P.; Ottewill, R. H. A neutron scattering study of the structure of a bimodal colloidal crystal. *J. Chem. Phys.* **1992**, *96*, 3306–3318.

(58) Qiao, B.; Demars, T.; Olvera de la Cruz, M.; Ellis, R. J. How hydrogen bonds affect the growth of reverse micelles around coordinating metal ions. *J. Phys. Chem. Lett.* **2014**, *5*, 1440–1444.

(59) Ellis, R. J.; Meridiano, Y.; Muller, J.; Berthon, L.; Guilbaud, P.; Zorz, N.; Antonio, M. R.; Demars, T.; Zemb, T. Complexation-induced supramolecular assembly drives metal-ion extraction. *Chem. –Eur. J.* **2014**, *20*, 12796–12807.

(60) Qiao, B. F.; Ferru, G.; Olvera de la Cruz, M.; Ellis, R. J. Molecular origins of mesoscale ordering in a metalloamphiphile phase. *ACS Cent. Sci.* **2015**, *1*, 493–503.

(61) Sevick, E.; Monson, P.; Ottino, J. Monte-carlo calculations of cluster statistics in continuum models of composite morphology. *J. Chem. Phys*. **1988**, *88*, 1198–1206.

(62) Servis, M.; Wu, D.; Jenifer, S.; Clark, A. Square supramolecular assemblies of uranyl complexes in organic solvents. *Chem. Commun*. **2018**, *54*, 10064-10067.

(63) Hill, T. L. *An Introduction to Statistical Thermodynamics*; Addison-Wesley: Reading, MA, USA, 1960.

(64) Higgins, J. S.; Benoît, H.C. *Polymers and Neutron Scattering*. Oxford University Press: Oxford, 1994.

(65) Berthon, L.; Martinet, L.; Testard, F.; Madic, C.; Zemb, T. Solvent penetration and sterical stabilization of reverse aggregates based on the DIAMEX process extracting molecules: Consequences for the third phase formation. *Solvent. Extr. Ion Exch.* **2007,** *25*, 545–576.

(66) Zemb, T.; Bauer, C.; Bauduin, P.; Belloni, L.; Dejugnat, C.; Diat, O.; Dubois, V.; Dufreche, J. F.; Dourdain, S.; Duvail, M.; Larpent, C.; Testard, F.; Pellet-Rostaing, S. Recycling metals by controlled transfer of ionic species between complex fluids: en route to "ienaics". *Colloid Polym. Sci.* **2015,** *293*, 1–22.

(67) Abécassis, B.; Testard, F.; Zemb, T.; Berthon, L.; Madic, C. Effect of *n*-octanol on the structure at the supramolecular scale of concentrated dimethyldioctylhexylethoxymalonamide extractant solutions. *Langmuir* **2003,** *19*, 6638–6644.

(68) Whittaker, D.; Geist, A.; Modolo, G.; Taylor, R.; Sarsfield, M.; Wilden, A. Applications of diglycolamide based solvent extraction processes in spent nuclear fuel reprocessing, Part 1: TODGA. *Solvent Extr. Ion Exch.* **2018,** *36*, 223–256.

(69) Siczek, A. A.; Steindler, M. J. Chemistry of ruthenium and zirconium in the PUREX solvent-extraction process. *At. Energy Rev.* **1978**, *16*, 575–618.

(70) Alcock, K.; Bedford, F. C.; Hardwick, W. H.; McKay, H. A. C. Tri-*n*-butyl phosphate as an extracting solvent for inorganic nitrates—I Zirconium nitrate. *J. Inorg. Nucl. Chem.* **1957,** *4*, 100–105.

(71) Marushita, M.; Mitsui, T.; Fukuda, T.; Takahasi, M.; Inami, T.; Katayama, Y.; Shiwaku, H.; Mizuki, J. Diamond double-crystal monochromator in Bragg geometry installed on BL-11XU at SPring-8. *Nucl. Instrum. Methods Phys. Res. A* **2001**, *467*, 392–395.

(72) Ressler, T. WinXAS: a program for X-ray absorption spectroscopy data analysis under MS-Windows. *J. Synchr. Rad.* **1998,** *5*, 118–122.

(73) Zhao, J. K.; Gao, C. Y.; Liu, D. The extended Q-range small-angle neutron scattering diffractometer at the SNS. *J. Appl. Crystallogr.* **2010,** *43*, 1068–1077.

(74) Arnold, O.; Bilheux, J. C.; Borreguero, J. M.; Buts, A.; Campbell, S. I.; Chapon, L.; Doucet, M.; Draper, N.; Leal, R. F.; Gigg, M. A.; Lynch, V. E.; Markvardsen, A.; Mikkelson, D. J.; Mikkelson, R. L.; Miller, R.; Palmen, K.; Parker, P.; Passos, G.; Perring, T. G.; Peterson, P. F.; Ren, S.; Reuter, M. A.; Savici, A. T.; Taylor, J. W.; Taylor, R. J.; Tolchenoy, R.; Zhou, W.; Zikoysky, J. Mantid – Data analysis and visualization package for neutron scattering and μ SR experiments. *Nucl. Instrum. Methods Phys. Res. A* **2014**, *764*, 156–166.

(75) Wignall, G. D.; Bates, F. S. Absolute calibration of small-angle neutron-scattering data. *J. Appl. Crystallogr.* **1987**, *20*, 28–40.

(76) Rosov, N.; Rathgeber, S.; Monkenbusch, M. Scattering from polymers: Characterization by X-rays, neutrons, and light; *ACS Symposium Series*: **2000**, *789*, 103–116.

(77) Monkenbusch, M.; Schatzler, R.; Richter, D. The Jülich neutron spin-echo spectrometer - Design and performance. *Nucl. Instrum. Methods Phys. Res. A* 1997, *399*, 301–323.

(78) Frisch, M. J.; Trucks, G. W.; Schlegel, H. B.; Scuseria, G. E.; Robb, M. A.; Cheeseman, J. R.; Scalmani, G.; Barone, V.; Mennucci, B.; Petersson, G. A.; Nakatsuji, H.; Caricato, M.;

Li, X.; Hratchian, H. P.; Izmaylov, A. F.; Bloino, J.; Zheng, G.; Sonnenberg, J. L.; Hada, M.; Ehara, M.; Toyota, K.; Fukuda, R.; Hasegawa, J.; Ishida, M.; Nakajima, T.; Honda, Y.; Kitao, O.; Nakai, H.; Vreven, T.; Montgomery, J. A.; Jr.; Peralta, J. E.; Ogliaro, F.; Bearpark, M.; Heyd, J. J.; Brothers, E.; Kudin, K. N.; Staroverov, V. N.; Kobayashi, R.; Normand, J.; Raghavachari, K.; Rendell, A.; Burant, J. C.; Iyengar, S. S.; Tomasi, J.; Cossi, M.; Rega, N.; Millam, J. M.; Klene, M.; Knox, J. E.; Cross, J. B.; Bakken, V.; Adamo, C.; Jaramillo, J.; Gomperts, R.; Stratmann, R. E.; Yazyev, O.; Austin, A. J.; Cammi, R.; Pomelli, C.; Ochterski, J. W.; Martin, R. L.; Morokuma, K.; Zakrzewski, V. G.; Voth, G. A.; Salvador, P.; Dannenberg, J. J.; Dapprich, S.; Daniels, A. D.; Farkas, O.; Foresman, J. B.; Ortiz, J. V.; Cioslowski, J.; Fox, D. J. *Gaussian 09 Program*; Gaussian, Inc.: Wallingford, CT, 2009.

(79) Lee, C. T.; Yang, W. T.; Parr, R. G. Development of the Colle-Salvetti correlation-energy formula into a functional of the electron density. *Phys. Rev. B* **1988**, *37*, 785–789.

(80) Stephens, P. J.; Devlin, F. J.; Chabalowski, C. F.; Frisch, M. J. Ab-initio calculation of vibrational absorption and circular dichroism spectra using density functional force fields. *J. Phys. Chem.* **1994**, *98*, 11623–11627.

(81) Hay, P. J.; Wadt, W. R. *Ab initio* effective core potentials for molecular calculations. Potentials for the transition-metal atoms Sc to Hg. *J. Chem. Phys.* **1985**, *82*, 270–283.

(82) Hay, P. J.; Wadt, W. R. *Ab initio* effective core potentials for molecular calculations. Potentials for K to Au including the outermost core orbitals *J. Chem. Phys.* **1985**, *82*, 299–310.

(83) Caughlan, C. N.; Hart, F. A.; Vannice, R. Crystal and molecular structure of tetranitratobis(triphenylphosphine oxide)cerium(IV). *Inorg. Chem.* **1971**, *10*, 115–122.

(84) Tomasi, J.; Mennucci, B.; Cammi, R. Quantum mechanical continuum solvation models. *Chem. Rev.* **2005,** *105*, 2999–3093.

(85) Improta, R.; Santoro, F. Excited-state behavior of trans and cis isomers of stilbene and stiff stilbene: A TD-DFT study. *J. Phys. Chem. A* **2005,** *109*, 10058–10067.

(86) Weast, R. C. *CRC Handbook of Chemistry and Physics*, 76th ed.; CRC Press: Boca Raton, FL, 1995.

(87) Rappé, A. K.; Casewit, C. J.; Colwell, K. S.; Goddard Iii, W. A.; Skiff, W. M. Uff, a full periodic table force field for molecular mechanics and molecular dynamics simulations *J. Am. Chem. Soc.* **1992**, *114*, 10024–10035.

(88) Besler, B. H.; Merz, K. M.; Kollman, P. A. Atomic charges derived from semiempirical methods. *J. Comput. Chem.* **1990**, *11*, 431–439.

(89) Berendsen, H. J.; van der Spoel, D.; van Drunen, R. GROMACS: A message-passing parallel molecular dynamics implementation. *Comput. Phys. Commun.* **1995**, *91*, 43−56.

(90) Mu, J.; Motokawa, R.; Williams, C. D.; Akutsu, K.; Shotaro, N.; Masters, A. J. Comparative molecular dynamics study on tri-*n*-butyl phosphate in organic and aqueous environments and its relevance to nuclear extraction processes. *J. Phys. Chem. B* **2016**, *120*, 5183–5193.

(91) Guilbaud, P.; Wipff, G. Hydration of UO_2^{2+} cation and its NO_3^- and 18-crown-6 adducts studied by molecular dynamics simulations. *J. Phys. Chem.*, **1993**, *97*, 5685–5692.

(92) Li, P. F.; Song, L. F.; Merz, K. M. Parameterization of highly charged metal ions using the 12-6-4 LJ-type nonbonded model in explicit water. *J. Phys. Chem. B* **2015**, *119*, 883−895.

(93) Sambasivarao, S. V.; Acevedo, O. Development of OPLS-AA force field parameters for 68 unique ionic liquids. *J. Chem. Theory Comput.* **2009**, *5*, 1038–1050.

(94) Banks, J. L.; Beard, H. S.; Cao, Y. X.; Cho, A. E.; Damm, W.; Farid, R.; Felts, A. K.; Halgren, T. A.; Mainz, D. T.; Maple, J. R.; Murphy, R.; Philipp, D. M.; Repasky, M. P.; Zhang, L. Y.; Berne, B. J.; Friesner, R. A.; Gallicchio, E.; Levy, R. M. Integrated modeling program, applied chemical theory (IMPACT). *J. Comput. Chem.* **2005**, *26*, 1752–1780.

(95) Jorgensen, W. L.; Chandrasekhar, J.; Madura, J. D.; Impey, R. W.; Klein, M. L. Comparison of simple potential functions for simulating liquid water. *J. Chem. Phys.* **1983**, *79*, 926–935.

(96) Price, M. L.; Ostrovsky, D.; Jorgensen, W. L. Gas-phase and liquid-state properties of esters, nitriles, and nitro compounds with the OPLS-AA force field. *J. Comput. Chem.* **2001**, *22*, 1340–1352.

(97) Hockney, R. W. Potential calculation and some applications. *Methods Comput. Phys.* **1970**, *9*, 136–211.

(98) Van Der Spoel, D.; van Maaren, P. J. The origin of layer structure artifacts in simulations of liquid water. *J. Chem. Theor. Comput.* **2006**, *2*, 1–11.

(99) Darden, T.; York, D.; Pedersen, L. Particle mesh Ewald: an $N\cdot\mathrm{Log}(N)$ method for Ewald sums in large systems. *J. Chem. Phys.* **1993**, *98*, 10089–10092.

(100) Bussi, G.; Donadio, D.; Parrinello, M. Canonical sampling through velocity rescaling. *J. Chem. Phys.* **2007**, *126*, 014101.

(101) Berendsen, H. J.; Postma, J. P. M.; van Gunsteren, W. F.; DiNola, A. R. H. J.; Haak, J. R. Molecular dynamics with coupling to an external bath. *J. Chem. Phys.* **1984**, *81*, 3684–3690.

(102) Nosé, S. A unified formulation of the constant temperature molecular dynamics methods. *J. Chem. Phys.* **1984**, *81*, 511–519.

(103) Hoover, W. G. Canonical dynamics: Equilibrium phase-space distributions. *Phys. Rev. A* **1985**, *31*, 1695–1967.

(104) Parrinello, M.; Rahman, A. Polymorphic transitions in single crystals: A new molecular dynamics method. *J. Appl. Phys.* **1981**, *52*, 7182–7190.

(105) Kotlarchyk, M.; Chen, S. H. Analysis of small angle neutron scattering spectra from polydisperse interacting colloids. *J. Chem. Phys.* **1983,** *79*, 2461–2469.

(106) Brown, P.J.; Fox A.G.; Maslen, E.N.; O'Keefe, M.A; Willis. B.T.M. *International Tables for Crystallography.* **2006**, *C*, 554–595.

(107) Motokawa, R.; Kobayashi, T.; Endo, H.; Ikeda, T.; Yaita, T.; Suzuki, S.; Narita, H.; Akutsu, K.; Heller, W. T. Small-angle neutron scattering study of specific interaction and coordination structure formed by mono-acetyl-substituted dibenzo-20-crown-6-ether and cesium ions. *J. Nucl. Sci. Technol.* **2016**, *53*, 1205–1211.

(108) Morozov, I. V.; Fedorova, A. A.; Palamarchuk, D. V.; Troyanov, S. I. Synthesis and crystal structures of zirconium(IV) nitrate complexes $(NO_2)[Zr(NO_3)_3(H_2O)_3]_2(NO_3)_3$, $Cs[Zr(NO_3)_5]$, and $(NH_4)[Zr(NO_3)_5](HNO_3)$. *Russ. Chem. B* **2005,** *54*, 93–98.

12. GROMACS input files

```
[ moleculetype ]
ZrCpx    3


[ atoms ]

; nr     type     resnr    resid    atom     cgnr     charge
1        Zr       1       ZrCpx       Zr    1        2.767
2         P       1       ZrCpx        P    2        0.909
3        OS       1       ZrCpx       OS    3       -0.320
4        OS       1       ZrCpx       OS    4       -0.397
5        OS       1       ZrCpx       OS    5       -0.331
6        O2       1       ZrCpx       O2    6       -0.616
7         C       1       ZrCpx        C    7        0.114
8         C       1       ZrCpx        C    8       -0.063
9         C       1       ZrCpx        C    9        0.168
10        C       1       ZrCpx        C   10       -0.335
11        C       1       ZrCpx        C   11        0.194
12        C       1       ZrCpx        C   12       -0.058
13        C       1       ZrCpx        C   13        0.072
14        C       1       ZrCpx        C   14       -0.206
15        C       1       ZrCpx        C   15       -0.030
16        C       1       ZrCpx        C   16        0.003
17        C       1       ZrCpx        C   17        0.053
18        C       1       ZrCpx        C   18       -0.246
19        H       1       ZrCpx        H   19        0.009
20        H       1       ZrCpx        H   20        0.081
21        H       1       ZrCpx        H   21        0.041
22        H       1       ZrCpx        H   22        0.039
23        H       1       ZrCpx        H   23       -0.004
24        H       1       ZrCpx        H   24       -0.017
25        H       1       ZrCpx        H   25        0.087
26        H       1       ZrCpx        H   26        0.083
27        H       1       ZrCpx        H   27        0.080
28        H       1       ZrCpx        H   28        0.071
29        H       1       ZrCpx        H   29        0.026
30        H       1       ZrCpx        H   30        0.019
31        H       1       ZrCpx        H   31        0.030
32        H       1       ZrCpx        H   32       -0.004
33        H       1       ZrCpx        H   33        0.013
34        H       1       ZrCpx        H   34        0.061
35        H       1       ZrCpx        H   35        0.051
36        H       1       ZrCpx        H   36        0.044
37        H       1       ZrCpx        H   37        0.118
38        H       1       ZrCpx        H   38        0.073
39        H       1       ZrCpx        H   39        0.035
40        H       1       ZrCpx        H   40        0.049
41        H       1       ZrCpx        H   41        0.009
42        H       1       ZrCpx        H   42        0.019
43        H       1       ZrCpx        H   43        0.071
```

44	H	1	ZrCpx	H	44	0.063
45	H	1	ZrCpx	H	45	0.063
46	P	1	ZrCpx	P	46	1.016
47	OS	1	ZrCpx	OS	47	-0.310
48	OS	1	ZrCpx	OS	48	-0.396
49	OS	1	ZrCpx	OS	49	-0.411
50	O2	1	ZrCpx	O2	50	-0.497
51	C	1	ZrCpx	C	51	-0.080
52	C	1	ZrCpx	C	52	0.023
53	C	1	ZrCpx	C	53	0.101
54	C	1	ZrCpx	C	54	-0.330
55	C	1	ZrCpx	C	55	0.100
56	C	1	ZrCpx	C	56	-0.055
57	C	1	ZrCpx	C	57	0.124
58	C	1	ZrCpx	C	58	-0.283
59	C	1	ZrCpx	C	59	0.074
60	C	1	ZrCpx	C	60	-0.186
61	C	1	ZrCpx	C	61	0.169
62	C	1	ZrCpx	C	62	-0.325
63	H	1	ZrCpx	H	63	0.101
64	H	1	ZrCpx	H	64	0.070
65	H	1	ZrCpx	H	65	0.015
66	H	1	ZrCpx	H	66	0.048
67	H	1	ZrCpx	H	67	0.004
68	H	1	ZrCpx	H	68	0.013
69	H	1	ZrCpx	H	69	0.081
70	H	1	ZrCpx	H	70	0.080
71	H	1	ZrCpx	H	71	0.086
72	H	1	ZrCpx	H	72	-0.008
73	H	1	ZrCpx	H	73	0.083
74	H	1	ZrCpx	H	74	0.053
75	H	1	ZrCpx	H	75	0.027
76	H	1	ZrCpx	H	76	0.003
77	H	1	ZrCpx	H	77	-0.009
78	H	1	ZrCpx	H	78	0.068
79	H	1	ZrCpx	H	79	0.076
80	H	1	ZrCpx	H	80	0.074
81	H	1	ZrCpx	H	81	0.109
82	H	1	ZrCpx	H	82	0.032
83	H	1	ZrCpx	H	83	0.092
84	H	1	ZrCpx	H	84	0.039
85	H	1	ZrCpx	H	85	-0.010
86	H	1	ZrCpx	H	86	0.001
87	H	1	ZrCpx	H	87	0.087
88	H	1	ZrCpx	H	88	0.079
89	H	1	ZrCpx	H	89	0.080
90	N	1	ZrCpx	N	90	0.835
91	O	1	ZrCpx	O	91	-0.583
92	O	1	ZrCpx	O	92	-0.365
93	O	1	ZrCpx	O	93	-0.617
94	N	1	ZrCpx	N	94	0.767
95	O	1	ZrCpx	O	95	-0.368
96	O	1	ZrCpx	O	96	-0.509
97	O	1	ZrCpx	O	97	-0.634

```
98       N       1      ZrCpx       N   98        0.867
99       O       1      ZrCpx       O   99       -0.384
100      O       1      ZrCpx       O  100       -0.643
101      O       1      ZrCpx       O  101       -0.591
102      N       1      ZrCpx       N  102        0.720
103      O       1      ZrCpx       O  103       -0.570
104      O       1      ZrCpx       O  104       -0.327
105      O       1      ZrCpx       O  105       -0.594


 [ bonds ]
; i      j       funct    b0       kb
1        6       6        2.179    418400.0
1        5       6        2.231    418400.0
1        91      6        2.312    418400.0
1        93      6        2.297    418400.0
1        96      6        2.499    418400.0
1        97      6        2.276    418400.0
1        100     6        2.316    418400.0
1        101     6        2.395    418400.0
1        103     6        2.382    418400.0
1        105     6        2.315    418400.0
2        3       1
2        4       1
2        5       1
2        6       1
3        7       1
4        11      1
5        15      1
7        8       1
7        19      1
7        20      1
8        9       1
8        21      1
8        22      1
9        10      1
9        23      1
9        24      1
10       25      1
10       26      1
10       27      1
11       12      1
11       28      1
11       29      1
12       13      1
12       30      1
12       31      1
13       14      1
13       32      1
13       33      1
14       34      1
14       35      1
14       36      1
15       16      1
```

```
15      37      1
15      38      1
16      17      1
16      39      1
16      40      1
17      18      1
17      41      1
17      42      1
18      43      1
18      44      1
18      45      1
46      47      1
46      48      1
46      49      1
46      50      1
47      51      1
48      55      1
49      59      1
51      52      1
51      63      1
51      64      1
52      53      1
52      65      1
52      66      1
53      54      1
53      67      1
53      68      1
54      69      1
54      70      1
54      71      1
55      56      1
55      72      1
55      73      1
56      57      1
56      74      1
56      75      1
57      58      1
57      76      1
57      77      1
58      78      1
58      79      1
58      80      1
59      60      1
59      81      1
59      82      1
60      61      1
60      83      1
60      84      1
61      62      1
61      85      1
61      86      1
62      87      1
62      88      1
62      89      1
```

```
90      91      1
90      92      1
90      93      1
94      95       1
94      96      1
94      97      1
98      99      1
98      100     1
98      101     1
102     103     1
102     104     1
102     105     1


 [ angles ]
; i     j       k       func    th0     cth
6       1       50      10      141.8   1255.2
6       1       91      10      134.6   1255.2
6       1       93      10      141.7   1255.2
6       1       97      10      82.6    1255.2
6       1       100     10      76.8    1255.2
6       1       101     10      71.5    1255.2
6       1       103     10      71.9    1255.2
6       1       105     10      97.6    1255.2
50      1       91      10      71.8    1255.2
50      1       93      10      73.1    1255.2
50      1       97      10      72.3    1255.2
50      1       100     10      140.6   1255.2
50      1       101     10      130.5   1255.2
50      1       103     10      126.7   1255.2
50      1       105     10      73.1    1255.2
91      1       93      10      55.6    1255.2
91      1       97      10      84.4    1255.2
91      1       100     10      72.1    1255.2
91      1       101     10      112.6   1255.2
91      1       103     10      141.7   1255.2
91      1       105     10      126     1255.2
93      1       97      10      133.5   1255.2
93      1       100     10      73.8    1255.2
93      1       101     10      71.6    1255.2
93      1       103     10      125.4   1255.2
93      1       105     10      75.6    1255.2
97      1       100     10      118.9   1255.2
97      1       101     10      154     1255.2
97      1       103     10      71.1    1255.2
97      1       105     10      121.5   1255.2
100     1       101     10      54.1    1255.2
100     1       103     10      145.6   1255.2
100     1       105     10      117.9   1255.2
101     1       103     10      101.4   1255.2
101     1       105     10      65.3    1255.2
103     1       105     10      54.3    1255.2
3       2       4       1
3       2       5       1
```

3	2	6	1
4	2	5	1
4	2	6	1
5	2	6	1
2	3	7	1
2	4	11	1
2	5	15	1
3	7	8	1
3	7	19	1
3	7	20	1
8	7	19	1
8	7	20	1
19	7	20	1
7	8	9	1
7	8	21	1
7	8	22	1
9	8	21	1
9	8	22	1
21	8	22	1
8	9	10	1
8	9	23	1
8	9	24	1
10	9	23	1
10	9	24	1
23	9	24	1
9	10	25	1
9	10	26	1
9	10	27	1
25	10	26	1
25	10	27	1
26	10	27	1
4	11	12	1
4	11	28	1
4	11	29	1
12	11	28	1
12	11	29	1
28	11	29	1
11	12	13	1
11	12	30	1
11	12	31	1
13	12	30	1
13	12	31	1
30	12	31	1
12	13	14	1
12	13	32	1
12	13	33	1
14	13	32	1
14	13	33	1
32	13	33	1
13	14	34	1
13	14	35	1
13	14	36	1
34	14	35	1
34	14	36	1

35	14	36	1
5	15	16	1
5	15	37	1
5	15	38	1
16	15	37	1
16	15	38	1
37	15	38	1
15	16	17	1
15	16	39	1
15	16	40	1
17	16	39	1
17	16	40	1
39	16	40	1
16	17	18	1
16	17	41	1
16	17	42	1
18	17	41	1
18	17	42	1
41	17	42	1
17	18	43	1
17	18	44	1
17	18	45	1
43	18	44	1
43	18	45	1
44	18	45	1
47	46	48	1
47	46	49	1
47	46	50	1
48	46	49	1
48	46	50	1
49	46	50	1
46	47	51	1
46	48	55	1
46	49	59	1
47	51	52	1
47	51	63	1
47	51	64	1
52	51	63	1
52	51	64	1
63	51	64	1
51	52	53	1
51	52	65	1
51	52	66	1
53	52	65	1
53	52	66	1
65	52	66	1
52	53	54	1
52	53	67	1
52	53	68	1
54	53	67	1
54	53	68	1
67	53	68	1
53	54	69	1
53	54	70	1

53	54	71	1
69	54	70	1
69	54	71	1
70	54	71	1
48	55	56	1
48	55	72	1
48	55	73	1
56	55	72	1
56	55	73	1
72	55	73	1
55	56	57	1
55	56	74	1
55	56	75	1
57	56	74	1
57	56	75	1
74	56	75	1
56	57	58	1
56	57	76	1
56	57	77	1
58	57	76	1
58	57	77	1
76	57	77	1
57	58	78	1
57	58	79	1
57	58	80	1
78	58	79	1
78	58	80	1
79	58	80	1
49	59	60	1
49	59	81	1
49	59	82	1
60	59	81	1
60	59	82	1
81	59	82	1
59	60	61	1
59	60	83	1
59	60	84	1
61	60	83	1
61	60	84	1
83	60	84	1
60	61	62	1
60	61	85	1
60	61	86	1
62	61	85	1
62	61	86	1
85	61	86	1
61	62	87	1
61	62	88	1
61	62	89	1
87	62	88	1
87	62	89	1
88	62	89	1
91	90	92	1
91	90	93	1

```
92      90      93      1
95      94      96      1
95      94      97      1
96      94      97      1
99      98      100     1
99      98      101     1
100     98      101     1
103     102     104     1
103     102     105     1
104     102     105     1


 [ dihedrals ]
; i      j       k       l       func    th0     cth     mult
2       3       7       8       5
2       3       7       19      5
2       3       7       20      5
2       4       11      12      5
2       4       11      28      5
2       4       11      29      5
2       5       15      16      5
2       5       15      37      5
2       5       15      38      5
3       2       4       11      5
3       2       5       15      5
3       7       8       9       5
3       7       8       21      5
3       7       8       22      5
4       2       3       7       5
4       2       5       15      5
4       11      12      13      5
4       11      12      30      5
4       11      12      31      5
5       2       3       7       5
5       2       4       11      5
5       15      16      17      5
5       15      16      39      5
5       15      16      40      5
6       2       3       7       5
6       2       4       11      5
6       2       5       15      5
7       8       9       10      5
7       8       9       23      5
7       8       9       24      5
8       9       10      25      5
8       9       10      26      5
8       9       10      27      5
9       8       7       19      5
9       8       7       20      5
10      9       8       21      5
10      9       8       22      5
11      12      13      14      5
11      12      13      32      5
11      12      13      33      5
```

12	13	14	34	5
12	13	14	35	5
12	13	14	36	5
13	12	11	28	5
13	12	11	29	5
14	13	12	30	5
14	13	12	31	5
15	16	17	18	5
15	16	17	41	5
15	16	17	42	5
16	17	18	43	5
16	17	18	44	5
16	17	18	45	5
17	16	15	37	5
17	16	15	38	5
18	17	16	39	5
18	17	16	40	5
19	7	8	21	5
19	7	8	22	5
20	7	8	21	5
20	7	8	22	5
21	8	9	23	5
21	8	9	24	5
22	8	9	23	5
22	8	9	24	5
23	9	10	25	5
23	9	10	26	5
23	9	10	27	5
24	9	10	25	5
24	9	10	26	5
24	9	10	27	5
28	11	12	30	5
28	11	12	31	5
29	11	12	30	5
29	11	12	31	5
30	12	13	32	5
30	12	13	33	5
31	12	13	32	5
31	12	13	33	5
32	13	14	34	5
32	13	14	35	5
32	13	14	36	5
33	13	14	34	5
33	13	14	35	5
33	13	14	36	5
37	15	16	39	5
37	15	16	40	5
38	15	16	39	5
38	15	16	40	5
39	16	17	41	5
39	16	17	42	5
40	16	17	41	5
40	16	17	42	5
41	17	18	43	5

41	17	18	44	5
41	17	18	45	5
42	17	18	43	5
42	17	18	44	5
42	17	18	45	5
46	47	51	52	5
46	47	51	63	5
46	47	51	64	5
46	48	55	56	5
46	48	55	72	5
46	48	55	73	5
46	49	59	60	5
46	49	59	81	5
46	49	59	82	5
47	46	48	55	5
47	46	49	59	5
47	51	52	53	5
47	51	52	65	5
47	51	52	66	5
48	46	47	51	5
48	46	49	59	5
48	55	56	57	5
48	55	56	74	5
48	55	56	75	5
49	46	47	51	5
49	46	48	55	5
49	59	60	61	5
49	59	60	83	5
49	59	60	84	5
50	46	47	51	5
50	46	48	55	5
50	46	49	59	5
51	52	53	54	5
51	52	53	67	5
51	52	53	68	5
52	53	54	69	5
52	53	54	70	5
52	53	54	71	5
53	52	51	63	5
53	52	51	64	5
54	53	52	65	5
54	53	52	66	5
55	56	57	58	5
55	56	57	76	5
55	56	57	77	5
56	57	58	78	5
56	57	58	79	5
56	57	58	80	5
57	56	55	72	5
57	56	55	73	5
58	57	56	74	5
58	57	56	75	5
59	60	61	62	5
59	60	61	85	5

59	60	61	86	5
60	61	62	87	5
60	61	62	88	5
60	61	62	89	5
61	60	59	81	5
61	60	59	82	5
62	61	60	83	5
62	61	60	84	5
63	51	52	65	5
63	51	52	66	5
64	51	52	65	5
64	51	52	66	5
65	52	53	67	5
65	52	53	68	5
66	52	53	67	5
66	52	53	68	5
67	53	54	69	5
67	53	54	70	5
67	53	54	71	5
68	53	54	69	5
68	53	54	70	5
68	53	54	71	5
72	55	56	74	5
72	55	56	75	5
73	55	56	74	5
73	55	56	75	5
74	56	57	76	5
74	56	57	77	5
75	56	57	76	5
75	56	57	77	5
76	57	58	78	5
76	57	58	79	5
76	57	58	80	5
77	57	58	78	5
77	57	58	79	5
77	57	58	80	5
81	59	60	83	5
81	59	60	84	5
82	59	60	83	5
82	59	60	84	5
83	60	61	85	5
83	60	61	86	5
84	60	61	85	5
84	60	61	86	5
85	61	62	87	5
85	61	62	88	5
85	61	62	89	5
86	61	62	87	5
86	61	62	88	5
86	61	62	89	5

```
ZrCpx
  105
    1ZrCpx   Zr    1  -0.044   0.046   0.112
    1ZrCpx    P    2   0.281  -0.053  -0.017
    1ZrCpx   OS    3   0.320  -0.198   0.031
    1ZrCpx   OS    4   0.410   0.037   0.007
    1ZrCpx   OS    5   0.252  -0.069  -0.172
    1ZrCpx   O2    6   0.162   0.010   0.051
    1ZrCpx    C    7   0.338  -0.233   0.174
    1ZrCpx    C    8   0.484  -0.225   0.214
    1ZrCpx    C    9   0.503  -0.267   0.361
    1ZrCpx    C   10   0.650  -0.261   0.405
    1ZrCpx    C   11   0.402   0.182   0.027
    1ZrCpx    C   12   0.393   0.257  -0.105
    1ZrCpx    C   13   0.379   0.409  -0.086
    1ZrCpx    C   14   0.500   0.477  -0.020
    1ZrCpx    C   15   0.327  -0.156  -0.263
    1ZrCpx    C   16   0.454  -0.091  -0.314
    1ZrCpx    C   17   0.525  -0.179  -0.417
    1ZrCpx    C   18   0.654  -0.115  -0.471
    1ZrCpx    H   19   0.274  -0.168   0.234
    1ZrCpx    H   20   0.299  -0.335   0.180
    1ZrCpx    H   21   0.543  -0.289   0.148
    1ZrCpx    H   22   0.520  -0.122   0.200
    1ZrCpx    H   23   0.442  -0.202   0.426
    1ZrCpx    H   24   0.465  -0.369   0.375
    1ZrCpx    H   25   0.660  -0.292   0.510
    1ZrCpx    H   26   0.690  -0.160   0.396
    1ZrCpx    H   27   0.712  -0.328   0.344
    1ZrCpx    H   28   0.493   0.206   0.082
    1ZrCpx    H   29   0.315   0.203   0.090
    1ZrCpx    H   30   0.306   0.221  -0.161
    1ZrCpx    H   31   0.481   0.234  -0.166
    1ZrCpx    H   32   0.288   0.430  -0.029
    1ZrCpx    H   33   0.363   0.454  -0.185
    1ZrCpx    H   34   0.487   0.585  -0.017
    1ZrCpx    H   35   0.592   0.456  -0.075
    1ZrCpx    H   36   0.515   0.443   0.083
    1ZrCpx    H   37   0.256  -0.175  -0.344
    1ZrCpx    H   38   0.347  -0.251  -0.211
    1ZrCpx    H   39   0.521  -0.071  -0.229
    1ZrCpx    H   40   0.429   0.006  -0.358
    1ZrCpx    H   41   0.457  -0.199  -0.501
    1ZrCpx    H   42   0.548  -0.277  -0.373
    1ZrCpx    H   43   0.702  -0.180  -0.544
    1ZrCpx    H   44   0.725  -0.097  -0.390
    1ZrCpx    H   45   0.633  -0.019  -0.519
    1ZrCpx    P   46  -0.370  -0.014  -0.046
    1ZrCpx   OS   47  -0.351  -0.134  -0.146
    1ZrCpx   OS   48  -0.404   0.109  -0.140
    1ZrCpx   OS   49  -0.502  -0.048   0.034
    1ZrCpx   O2   50  -0.255   0.010   0.050
    1ZrCpx    C   51  -0.264  -0.126  -0.265
    1ZrCpx    C   52  -0.228  -0.268  -0.305
```

```
 1ZrCpx    C   53  -0.139  -0.271  -0.430
 1ZrCpx    C   54  -0.103  -0.413  -0.473
 1ZrCpx    C   55  -0.408   0.248  -0.093
 1ZrCpx    C   56  -0.355   0.336  -0.204
 1ZrCpx    C   57  -0.356   0.485  -0.164
 1ZrCpx    C   58  -0.299   0.575  -0.274
 1ZrCpx    C   59  -0.501  -0.113   0.166
 1ZrCpx    C   60  -0.483  -0.264   0.156
 1ZrCpx    C   61  -0.590  -0.335   0.073
 1ZrCpx    C   62  -0.571  -0.487   0.069
 1ZrCpx    H   63  -0.321  -0.075  -0.342
 1ZrCpx    H   64  -0.175  -0.068  -0.240
 1ZrCpx    H   65  -0.176  -0.316  -0.221
 1ZrCpx    H   66  -0.320  -0.325  -0.323
 1ZrCpx    H   67  -0.191  -0.220  -0.513
 1ZrCpx    H   68  -0.048  -0.213  -0.411
 1ZrCpx    H   69  -0.192  -0.472  -0.497
 1ZrCpx    H   70  -0.049  -0.466  -0.394
 1ZrCpx    H   71  -0.039  -0.412  -0.562
 1ZrCpx    H   72  -0.346   0.257  -0.003
 1ZrCpx    H   73  -0.512   0.270  -0.068
 1ZrCpx    H   74  -0.416   0.321  -0.294
 1ZrCpx    H   75  -0.253   0.305  -0.229
 1ZrCpx    H   76  -0.298   0.498  -0.072
 1ZrCpx    H   77  -0.459   0.516  -0.141
 1ZrCpx    H   78  -0.356   0.566  -0.367
 1ZrCpx    H   79  -0.195   0.548  -0.296
 1ZrCpx    H   80  -0.301   0.680  -0.244
 1ZrCpx    H   81  -0.598  -0.087   0.208
 1ZrCpx    H   82  -0.422  -0.067   0.226
 1ZrCpx    H   83  -0.484  -0.302   0.259
 1ZrCpx    H   84  -0.383  -0.287   0.116
 1ZrCpx    H   85  -0.589  -0.296  -0.029
 1ZrCpx    H   86  -0.689  -0.312   0.114
 1ZrCpx    H   87  -0.474  -0.514   0.026
 1ZrCpx    H   88  -0.649  -0.536   0.009
 1ZrCpx    H   89  -0.575  -0.530   0.170
 1ZrCpx    N   90  -0.219   0.189   0.269
 1ZrCpx    O   91  -0.168   0.236   0.161
 1ZrCpx    O   92  -0.300   0.249   0.336
 1ZrCpx    O   93  -0.175   0.072   0.300
 1ZrCpx    N   94   0.005   0.225  -0.103
 1ZrCpx    O   95   0.022   0.291  -0.203
 1ZrCpx    O   96   0.053   0.253   0.011
 1ZrCpx    O   97  -0.065   0.115  -0.104
 1ZrCpx    N   98   0.123   0.081   0.335
 1ZrCpx    O   99   0.200   0.099   0.426
 1ZrCpx    O  100   0.079   0.176   0.260
 1ZrCpx    O  101   0.078  -0.034   0.302
 1ZrCpx    N  102  -0.083  -0.225   0.061
 1ZrCpx    O  103  -0.042  -0.145  -0.030
 1ZrCpx    O  104  -0.107  -0.342   0.040
 1ZrCpx    O  105  -0.096  -0.170   0.176
1.00000   1.00000   1.00000
```